nature methods

Article

https://doi.org/10.1038/s41592-025-02865-2

Whole-brain reconstruction of fiber tracts based on cytoarchitectonic organization

Received: 7 October 2024

Accepted: 12 September 2025

Published online: 03 November 2025

Check for updates

Yue Zhang[1,2,13], Tao Song[2,3,13], Chao-Yu Yang[1,13], Yan Shen[1], Yi Yang[1], Xiaowei Hu[1], Rubin Zhao[1,4], Weibo Wang[1,2], Xin Wang[3], Hean Liu[3], Haotian Yan[3], Chunyun Jia[5], Yang Liu[1,2], Xueyan Wu[6], Huizhi Huang[7], Xintian Hu[8], Jiang-Ning Zhou[9], Liming Tan[5], Pak-Ming Lau[1], Hao Wang[10], Mu-Ming Poo[3], Pengcheng Zhou[1,4], Guo-Qiang Bi[1,5,11] ✉, Yanyang Xiao[1,2,5] ✉, Cirong Liu[2,3,12] ✉ & Fang Xu[1,2,4,5] ✉

Mapping of axon trajectories is crucial for understanding brain organization. Using whole-brain high-throughput fluorescence imaging, we developed a cytoarchitecture-based link estimation (CABLE) method for accurate fiber tract mapping at cellular resolution. This method infers the fiber direction from the inherent anisotropy of the nucleus or soma shape and spatial arrangement of adjacent cells. The inferred fiber tracts were validated by tracing virally labeled individual axons in the monkey brain. This CABLE method could disentangle complex intersecting or bending fibers that were uncertain in diffusion magnetic resonance imaging tractography, allowing accurate brain-wide fiber tract reconstruction in marmoset and macaque brains. Finally, we applied CABLE for rapid mapping of axon fiber abnormalities in diseased neonatal human brain tissues, establishing a path for high-resolution brain mapping of fiber tracts in the human brain.

The diverse functions of the brain depend on the complex axon fiber tracts that enable communication among various brain regions. Precise mapping of these tracts is essential for understanding the organization of neural circuits in normal and diseased brains[1,2]. Several techniques have been developed to map fiber tracts at millimeter to submillimeter resolution, including diffusion magnetic resonance imaging (dMRI)[3,4] and polarized light imaging (PLI)[5]. These methods estimate the fiber orientation distribution function (ODF) of the white matter by modeling the diffusion anisotropy of water molecules[6–8] or optical properties of myelin sheaths[9], respectively. Notably, the Nissl-based structure tensor (Nissl-ST)[10] analysis demonstrated that the in-plane organization of the tentative glial framework encodes high-resolution information about local fiber orientations. These methods have advanced our understanding of white matter structures and brain connectivity. However, these methods are limited in their capability of resolving intersecting fibers or bending fibers in complex white matter regions[4]. Moreover,

[1]Interdisciplinary Center for Brain Information, Brain Cognition and Brain Disease Institute, Shenzhen Institutes of Advanced Technology, Chinese Academy of Sciences, Shenzhen, China. [2]University of Chinese Academy of Sciences, Beijing, China. [3]Institute of Neuroscience, State Key Laboratory of Genetic Evolution and Animal Models, Center for Excellence in Brain Science and Intelligence Technology, International Center for Primate Brain Research, Chinese Academy of Sciences, Shanghai, China. [4]Faculty of Life and Health Sciences, Shenzhen University of Advanced Technology, Shenzhen, China. [5]Shenzhen-Hong Kong Institute of Brain Science, Shenzhen Institutes of Advanced Technology, Chinese Academy of Sciences, Shenzhen, China. [6]School of Basic Medicine, Anhui Medical University, Hefei, China. [7]Department of Neonatology, Anhui Provincial Children's Hospital/Children's Hospital Affiliated to Anhui Medical University, Hefei, China. [8]Key Laboratory of Animal Models and Human Disease Mechanism, Kunming Institute of Zoology, Chinese Academy of Sciences, Kunming, China. [9]Institute of Brain Science, The First Affiliated Hospital of Anhui Medical University, Hefei, China. [10]National Engineering Laboratory for Brain-inspired Intelligence Technology and Application, MoE Key Laboratory of Brain-inspired Intelligent Perception and Cognition, School of Information Science and Technology, University of Science and Technology of China, Hefei, China. [11]Hefei National Laboratory for Physical Sciences at the Microscale, and School of Life Sciences, University of Science and Technology of China, Hefei, China. [12]Shanghai Key Laboratory of Child Brain and Development, Shanghai, China. [13]These authors contributed equally: Yue Zhang 张越, Tao Song 宋韬, Chao-Yu Yang 杨朝宇. ✉e-mail: gqbi@ustc.edu.cn; yy.xiao@siat.ac.cn; crliu@ion.ac.cn; fang.xu@siat.ac.cn

the accuracy of ODFs and deduced fiber tractography depends on the biophysical models used and thus needs to be validated by histological axonal tracing, ideally in the same brain samples[11]. To validate ODFs or tractography results, previous studies relied on myelin or neurofilament staining[8,12] or viral tracing of specific fiber bundles[13] over limited brain regions. These validation methods lacked the resolution of single axons in three dimensions and the precise co-registration of cross-modal datasets[14]. Thus, there is a need for methods that can provide more precise and validated three-dimensional (3D) mapping of axon fibers over the entire brain.

Here we developed a CABLE method for determining 3D patterns of fiber tracts over the entire brain. We combined thick-tissue sectioning and clearing with high-speed fluorescence volumetric imaging[15,16] to reconstruct primate brain volumes at the micrometer resolution. We then used inherent 3D oriented features of the shape of individual somata or nuclei and their spatial arrangements detected in these whole-brain images (termed 'cytoarchitectonic orientation') to deduce fiber orientation and reconstruct fiber tracts throughout the entire primate brain. Using the Stereo-seq method[17] for single-cell spatial transcriptomics, we demonstrated that the cytoarchitectural features related to axon orientation were most prominent in oligodendrocytes within the white matter and neurons in the gray matter, and could be detected to various degrees in almost all cell types, as also validated by immunostaining. By applying cellular staining and brain-wide viral tracing of individual axons in the same brain, we demonstrated that the cytoarchitectonic orientation accurately represents the orientation of adjacent axons, including those in regions with complex fiber intersections or bending. The CABLE method overcame the limitations of traditional fiber tractography in such regions and is scalable across brains of varying sizes. We further applied CABLE to postmortem human brain tissue, demonstrating its applicability in detecting fiber tract impairment associated with neonatal hypoxic–ischemic encephalopathy (HIE). This 3D high-resolution whole-brain fiber tract mapping method, along with the multimodal datasets created during this study, provides a rich resource for future studies of the complex organization of primate brains.

Results

Whole-brain imaging reveals fiber-associated architectonic orientation in the primate brain

Glial cells are spatially organized in rows in the brain[18,19], suggesting they may be arranged along the axon fibers and thus could be used to estimate fiber orientation. To comprehensively map the 3D cytoarchitecture across the entire brain of various primate species, we used the integrative 'serial sectioning, 3D microscopy, semiautomated reconstruction and tracing' (SMART) pipeline for high-throughput and high-resolution data acquisition of the primate brain[16] (Fig. 1a). Brain samples were sectioned into 300-µm-thick slices, cleared by a primate-optimized uniform tissue clearing method, stained with the nucleus dye DAPI or NeuroTrace 640/660 (NT640; a fluorescent dye for Nissl bodies), and imaged using 'volumetric imaging with synchronized on-the-fly-scan and readout' (VISoR)[15]. Multichannel high-throughput fluorescence images of all slices of a macaque brain were acquired within 100 h per channel at a resolution of $1 \times 1 \times 2.5\ \mu m^3$, allowing rapid mapping and detailed analysis of cytoarchitecture.

In both white and gray matter, 3D imaging revealed the local anisotropy of cytoarchitectonic organization at multiple scales, primarily reflected by the linear arrangement of cells and the regular orientation of individual cells and their nuclei (Supplementary Fig. 1 and Supplementary Video 1). The organized cytoarchitectonic orientation coincided with known fiber orientations in regions with varying degrees of fiber intersecting. For example, in the corpus callosum where most fibers are unidirectional, cells were arranged in rows along the direction of fiber bundles (Fig. 1b), as revealed by Nissl-ST analysis[10]. Notably, segmented individual cells also showed ellipsoidal soma shapes, with their major axis oriented in the same direction, suggesting that both cell arrangement and soma morphology could serve as indicators of fiber orientation. Adjacent to the corpus callosum, the cingulum fiber bundle predominantly runs in the anterior–posterior direction[20], but intersects with other fibers oriented in the left–right direction, as presented in virus-tracing images (Supplementary Fig. 2). The 3D images faithfully revealed both anterior–posterior and left–right orientations of cell arrangements and soma shapes, as visualized in the sagittal and coronal planes, reflecting cingulum and intersecting fibers, respectively (Fig. 1c). In the corona radiata, known for its complex tri-directional fiber intersections[2,20], most cells aligned along the inferior–superior axis, corresponding to major projection pathways seen in coronal and sagittal views (Fig. 1d). Soma shapes were also oriented along the left–right and anterior–posterior axes, reflecting the presence of commissural and association fibers, respectively, while these orientations were not resolved by structure tensor analysis (Fig. 1d). These examples demonstrate that both cellular arrangement and soma shape anisotropy, visualized only through volumetric cytoarchitectonic imaging at cellular resolution, contain information about fiber orientations. Furthermore, it reveals individual cellular anisotropy contains finer orientation information than the cellular arrangement analyzed with structure tensor-based analysis, which may be particularly useful for resolving intersecting fibers in regions with complex fiber intersections.

To extract fiber orientations from this cell-intrinsic anisotropy, we developed the three-step CABLE method (Extended Data Fig. 1). First, we computed image gradients per pixel in high-resolution cytoarchitecture images to capture local directional features. Second, we constructed a directional scattering density function (DSDF) that aggregates these gradient signals within a local analysis window (the DSDF voxel), capturing orientation information from both cell arrangement and soma shape. Finally, given the conceptual similarity between DSDF and dMRI signals, both of which exhibit higher intensity perpendicular to fiber directions, we applied spherical deconvolution[21,22] to derive the cytoarchitectonic orientation distribution function (cODF) from the DSDF. This approach parallels methods used in dMRI to estimate fiber ODFs, with adaptations to our high-resolution image data (Supplementary Figs. 3 and 4 and Supplementary Note 1). This approach also works with nucleus-stained or autofluorescence images, although Nissl-stained images yield the best orientation estimates (Supplementary Figs. 5 and 6).

Unlike structure tensor analysis, which estimates only a single dominant orientation per analysis window, CABLE captures multiple cellular orientations within each window, making it more accurate for resolving complex fiber geometries (Extended Data Fig. 2). Moreover, beyond the spatial arrangement used in Nissl-ST, CABLE incorporates anisotropy of soma or nucleus shape into the DSDF, providing critical high-resolution directional cues. Removing this shape information reduced orientation coherence (Extended Data Fig. 3), underscoring its contribution to accurate fiber reconstruction.

Using this CABLE method, we acquired high-resolution mapping for whole-brain data of macaques, marmosets and humans (Supplementary Fig. 7). The cODFs accurately depicted white matter fibers oriented in various directions, visualized as elongated spheres with color-coded orientations (Fig. 1e): for example, projection fibers in the internal capsule, oriented in an inferior–superior direction, were visualized in blue; commissural fibers of the corpus callosum, extending left–right, were shown in red; and association fibers in the cingulum, projecting in the anterior–posterior direction, appeared in green. The intersection of the lenticular fasciculus and the internal capsule in the region of Edinger's comb clearly showed crossing fibers as reported previously[10]. Moreover, cODFs effectively depicted fiber orientations in both subcortical and cortical regions. For example, a recent study identified commissural fiber pathways within the rodent thalamus[23]; our cODF analysis revealed similar thalamic commissures in the primate brain (Extended Data Fig. 4). In the cortex, most axons

https://doi.org/10.1038/s41592-025-02865-2

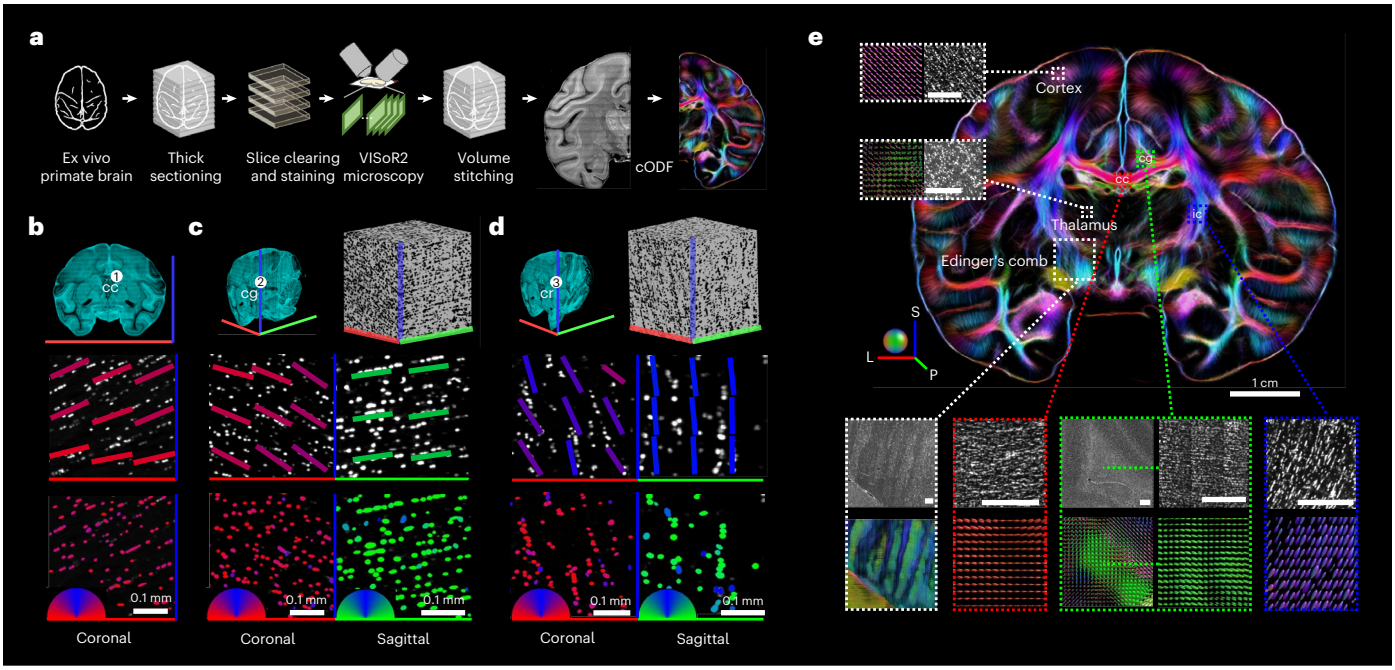

Fig. 1 | Cytoarchitectonic orientation in the macaque brain. a, Overview of the CABLE pipeline, including tissue sectioning and staining, VISoR microscopy imaging, 3D stitching and reconstruction of imaged sections, determination of 3D fiber orientation and subsequent fiber tractography. **b**–**d**, Cellular arrangements and soma morphologies in the corpus callosum (cc; **b**), cingulum (cg; **c**), and corona radiata (cr; **d**). Top row: anatomical location and corresponding Nissl-stained volume (inverted grayscale). Middle row: color-coded spatial orientations of cellular arrangements. Bottom row: color-coded orientations of segmented soma shapes. In **d**, soma shapes exhibit left–right and anterior–posterior orientations that are not captured by the cell arrangement analysis. **e**, A representative section of the 3D cODF map of a macaque brain reconstructed using CABLE. Insets highlight selected brain regions, each showing the cODF map alongside the corresponding Nissl-stained cytoarchitecture image for direct comparison. Scale bars in insets, 0.5 mm. In **b**–**e**, axes, short lines, soma masks and cODFs follow a consistent orientation color code: red for left–right, green for anterior–posterior, and blue for inferior–superior. This scheme is applied consistently across all figures unless otherwise noted.

are oriented perpendicular to the cortical surface in alignment with the organization of cortical columns. This orientation was also accurately reflected by the cODFs (Fig. 1e and Extended Data Fig. 4). Such precision is crucial for estimating anatomical connectivity through cODF-based tractography, as it enables tracking of connections that originate and terminate within the gray matter[24].

Diverse cell types reflect cytoarchitectonic orientation coherence

Given the diverse cell types in white and gray matter, we further examined which cell types contribute to the cytoarchitectonic orientation. We used the single-cell spatial transcriptome method 'Stereo-seq'[17] to assess the spatial configurations of various cell types in the marmoset brain. Two coronal and one sagittal Stereo-seq sections were obtained from two marmosets. Major cell types, including neurons and four glial cell types (oligodendrocytes, oligodendrocyte progenitor cells, astrocytes and microglia), were annotated using a previously published single-nucleus RNA sequencing (snRNA-seq) dataset on the marmoset brain[25]. Cell types in our Stereo-seq sections were identified by matching local gene expression profiles to the snRNA-seq dataset using a supervised method[26] (Supplementary Fig. 8 and Extended Data Fig. 5). The orientation of each cell was determined as the major axis of the ellipse fitted to their nucleus contour, segmented from single-stranded DNA (ssDNA) staining images of these sections (Supplementary Fig. 9). Due to the two-dimensional (2D) nature of Stereo-seq sections, we focused on brain areas where the fibers mainly oriented parallel to the section. Specifically, we examined the white matter regions of the corpus callosum and the fimbria in coronal sections (Fig. 2a,b), which exhibited dominant in-plane fiber orientations in left–right and inferior–superior directions, respectively[20]. Our results showed that the local orientations among most glial cells in local white matter regions were largely consistent (Supplementary Fig. 10). To quantify the consistency of each cell's orientation for inferring predominant fiber direction, we calculated the orientation coherence by comparing the orientation of each cell to the locally averaged cytoarchitectonic orientation. The four glial cell types exhibited nearly identical high orientation coherence in white matter regions (Fig. 2c and Extended Data Fig. 6a,b), indicating that the cytoarchitectonic orientation in the white matter is not cell-type specific.

We further evaluated the cytoarchitectonic orientation coherence in the cortex. Despite the slightly lower coherence compared to the white matter (Extended Data Fig. 6c and Supplementary Fig. 10e), most cells oriented along cortical columns, with their average orientation changing gradually along a tangential axis parallel to the pial surface (Fig. 2d and Extended Data Fig. 5a,b). While all cortical cells exhibited high orientation coherence, neurons showed slightly higher coherence than glial cells in the cortex (Extended Data Figs. 5c and 6d). We further examined the cytoarchitectonic orientation of 18 subtypes (9 glutamatergic and 9 GABAergic) of cortical neurons (Extended Data Fig. 5d–g). The analysis revealed that these subtypes displayed distinct layer preferences (Fig. 2e and Extended Data Fig. 5g) and slightly varied in their orientation coherence value (Supplementary Fig. 11). For example, two *Vip*-expressing GABAergic subtypes in layers I and II showed greater orientation coherence than other GABAergic neurons, and two *Rorb*-expressing glutamatergic subtypes in layer IV and layer V exhibited lower orientation coherence than other glutamatergic neurons. Despite these small variations, all neuron subtypes consistently showed substantially high orientation coherence in all three brain sections used in this study with only one exception with small sample size (subtype 08_I in section T472, $n = 30$; Fig. 2f and Extended Data Fig. 6e). These findings indicated that there is a strong inherent cytoarchitectonic orientation coherence of all cell types in both white and gray matter.

We further validated these findings using immunostaining for cell-type-specific markers across multiple brain regions. These analyses showed that the orientation of specific glial and neuronal cell types was consistently aligned with the local cytoarchitectonic orientation derived from all cells (Fig. 2g,h, Extended Data Fig. 7 and Supplementary Fig. 12). This alignment also corresponded well with known axonal orientations in the respective regions, suggesting that the cytoarchitectonic orientation likely reflects underlying axon organization.

Brain-wide axon tracing validates CABLE's inference of axon orientation

To investigate whether the coherent cytoarchitectonic orientation reflects the paths of neighboring axons on a whole-brain scale, we integrated CABLE mapping with virus-based axon tracing. Brain-wide neurite labeling was achieved by intravenous injection of an adeno-associated virus (AAV) capsid variant vector (AAV.CAP-B10)[27] that encodes a green fluorescent protein (GFP) and is capable of crossing the blood–brain barrier and sparsely infecting neurons (Fig. 3a, Supplementary Fig. 13 and Supplementary Video 2). The sample underwent multichannel VISoR imaging of GFP, DAPI and NT640 signals, as well as ex vivo dMRI analysis for comparison. Our multimodal data unveiled that the majority of glial cells encircling individual axons exhibited ellipsoidal nucleus shapes, organized spatially in parallel with axonal orientation. This was exemplified in the corpus callosum (Fig. 3b) and internal capsules (Fig. 3c). In regions where axons traversed two divergent paths, two corresponding patterns of cytoarchitectonic orientation in glial cells were observed, as illustrated in the cODFs generated via the CABLE technique (Fig. 3d). Furthermore, areas showcasing complex fiber configurations (Fig. 3e–h), such as white matter regions with triple-direction fiber intersections (Fig. 3f), gray matter zones with intertwined dendrites and axons (Fig. 3g) and thalamic nuclei with sparsely labeled axons (Fig. 3h), also consistently showed CABLE-extracted cytoarchitectonic orientations that aligned accurately with axon fiber trajectories (Supplementary Videos 2 and 3).

Our comprehensive multimodal dataset of the same specimen enabled a quantitative evaluation of the accuracy of various methods in determining fiber orientation by comparing the similarities between ODFs. The axonal orientation distribution functions (aODFs) across the brain from the brain-wide AAV tracing data were calculated using methods similar to those used for cODFs and set as the benchmark for comparison. Notably, cODFs exhibited higher similarity to aODFs than dMRI-derived orientation distribution functions (dODFs), as evidenced by their superior cosine similarity scores (Fig. 3i and Supplementary Fig. 14). For instance, in the corona radiata region characterized by complex tri-axial fiber intersections, the average cosine similarity score between aODFs and cODFs (0.84) was much higher than that between aODFs and dODFs (0.4) or between dODFs and cODFs (0.32; $P < 1 \times 10^{-300}$, two-sided Mann–Whitney U-test; Fig. 3i). The small discrepancy between cODFs and aODFs could be attributed in part to the extent of cell labeling, which was relatively sparse for axons but more ubiquitous for adjacent cells.

Our findings underscore CABLE's accuracy in deducing fiber orientation in comparison to dMRI. This was particularly evident for the macaque brain that exhibits complex fiber pathways. For instance, within the macaque occipital lobe, CABLE delineated the layered arrangement of white matter bundles, highlighting the separation between the stratum calcarinum and parahippocampal cingulum, which is a feature that was hardly discernible in dMRI images (Extended Data Fig. 8a). Additional instances include the ventral hippocampal commissure and the medial and lateral longitudinal striae (Extended Data Fig. 8b). Despite its small size in the primate brain[2], the ventral hippocampal commissure that connects bilateral hippocampi was clearly visualized by CABLE. The longitudinal striae axonal bundles within the indusium griseum, a dorsal hippocampal region often overlooked due to its small size[28], were also accurately depicted by CABLE, even in coronal sections where they appeared as through-plane fiber bundles that are difficult to discern in coronal PLI images (Extended Data Fig. 8c). In the cerebellum, CABLE shows a clearer depiction of lobar branching than dMRI (Extended Data Fig. 8d).

These examples showcase CABLE's capacity for mapping complex white matter structures, presenting substantial potential for

Fig. 2 | Single-cell spatial transcriptomics and immunostaining analysis reveal orientation coherence across different cell types. a, Visualization of cellular orientation of glial cells in a coronal Stereo-seq section of a marmoset brain. Glial cells are depicted as line segments with orientation and color representing cellular orientation. The corpus callosum and the fimbria are annotated with dashed borders. Bottom, cellular orientation maps of four glial cell types (oligodendrocytes (OLI), astrocytes (AST), oligodendrocyte progenitor cells (OPCs) and microglia (MIC)). **b**, ssDNA staining image of the corpus callosum and the fimbria areas (the solid boxes in **a**), displaying segmented cell masks with colors coded by their orientations. **c**, Top and middle, circular histograms of the orientation distribution of four cell types within the corpus callosum (top) and fimbria (middle). Colors code the median orientation within each area, which is also indicated by the white dashed lines. Bottom, distribution of orientation coherence for the four types of glial cells and the randomized simulation data. **d**, Left, visualization of the cellular orientation of neurons, with the arrowed line indicating the tangential axis of the cortex. Right, a 3D line showing the median orientations of neurons changing continuously along the tangential axis. The white-arrow line indicates the spatial position along the ascending tangential axis. The circular ring and the line color represent the median orientations of cells. **e**, Left, spatial distribution of all 18 subtypes of neurons. Right, 3D lines showing the orientations of each neuron subtype. The line colors code neuron subtypes. **f**, Distribution of orientation coherence values of all 18 subtypes of neurons and the randomized simulation data. Neuron subtypes are classified as shown in Extended Data Fig. 5d–g. In **c** and **f**, $^{***}P < 0.001$ (two-sided Mann–Whitney U-test). All cells from this section were included in the analysis. Sample sizes: OLI (n = 5,909), AST (202), OPCs (142), MIC (169), 01_I (728), 04_E (12,219), 17_E (1,716), 03_I (864), 18_E (842), 06_I (1,735), 16_E (1,997), 07_I (425), 02_I (129), 11_E (591), 09_I (1,730), 13_E (640), 14_E (535), 12_E (2,143), 05_I (787), 10_E (4,580), 15_I (272), 08_I (30), and random (254,530). Corresponding P values (versus random): $<1.0 \times 10^{-300}$, 3.1×10^{-34}, 8.0×10^{-20}, 4.9×10^{-23}, 1.0×10^{-61}, $<1.0 \times 10^{-300}$, 1.1×10^{-156}, 1.8×10^{-87}, 1.3×10^{-72}, 8.1×10^{-132}, 4.0×10^{-150}, 1.1×10^{-35}, 7.2×10^{-11}, 3.2×10^{-49}, 2.7×10^{-134}, 7.8×10^{-49}, 7.4×10^{-39}, 7.1×10^{-130}, 1.8×10^{-46}, 1.3×10^{-252}, 1.4×10^{-18} and 0.083, respectively. Embedded box plots in violin plots indicate the median (central white horizontal line) and the interquartile range (25th and 75th percentiles; box edges). Whiskers, minima and maxima outside this range are not shown. **g**, Co-staining across various brain regions. First column, co-staining of ASPA (green; mature oligodendrocyte marker) and SOX10 (magenta; pan-oligodendrocyte marker) in the marmoset anterior commissure (AC). Green dotted and magenta lines indicate the local orientations of all oligodendrocyte lineages ($SOX10^+$) and OPCs ($SOX10^+/ASPA^-$; magenta only), respectively. Second column, co-staining of glial fibrillary acidic protein (GFAP; astrocytes) and Nissl in the marmoset optic tract (OT). Red lines indicate local orientations of astrocytes (GFAP) and the overall cytoarchitecture (Nissl). Third column, co-staining of IBA1 (microglia) and DAPI in the mouse fimbria. Red lines show local orientations of microglia (IBA1) and overall cells (DAPI). Fourth column, co-staining of parvalbumin (PV; for PV^+ interneurons) and Nissl in the marmoset cortex. Red lines indicate the local orientations of PV^+ interneurons and the surrounding Nissl-stained cells. **h**, Quantification of orientation coherence in the four co-stained regions shown in **g**. No significant differences were observed between the specific cell types and the overall cytoarchitectonic orientation in any region (two-sided Mann–Whitney U-test; n = 36 (AC), 30 (OT), 30 (Fimbria), 30 (Cortex); P = 0.38, 0.75, 0.55 and 0.16, respectively). Violin plots show the distribution of orientation values using kernel density estimation. The embedded box plots indicate the median (central white horizontal line) and the interquartile range (25th and 75th percentiles; box edges), and the whiskers represent data within 1.5 times the interquartile range from the quartiles. Minima and maxima outside this range are not shown.

https://doi.org/10.1038/s41592-025-02865-2

addressing the complexities associated with intersecting fibers in fiber tractography[29,30].

CABLE enables accurate 3D reconstruction of complex white matter fiber tracts

The CABLE method utilizes directional image features (hereby, the gradients) to construct the cODF, serving as an analog to dMRI-derived ODFs, thereby compatible with well-established toolkits for tractography analysis[31] after minor adjustments. The high-precision cODF estimation enables the reconstruction of complex projection fibers through cODF-based CABLE tractography throughout the primate and human brains (Extended Data Fig. 9 and Supplementary Video 4), offering an effective method applicable for tackling challenging pathways previously resistant to existing techniques.

With its cellular resolution, CABLE is able to resolve trajectories with axonal turns. Our recent investigation observed sharp turns in primate white matter axonal fibers with a radius substantially smaller than dMRI voxels[16], posing challenges for dMRI in tracking these pathways. To evaluate CABLE's ability to track such turning fibers, we examined the corona radiata in the marmoset brain labeled by whole-brain viral tracing, where axonal trajectories exhibit sharp bends near the white–gray matter boundary (Supplementary Fig. 15a). Numerous axons ($n = 132$) were manually traced and categorized into three groups based on their medial-to-lateral positions within the corona radiata (Supplementary Video 5). With its high resolution, CABLE-derived tractography closely mirrored the actual axon fibers' trajectories (Fig. 4a). Fibers linked with cortical area 3 (A3) exhibited a primary concentration medially, fibers associated with parietal area PF or the

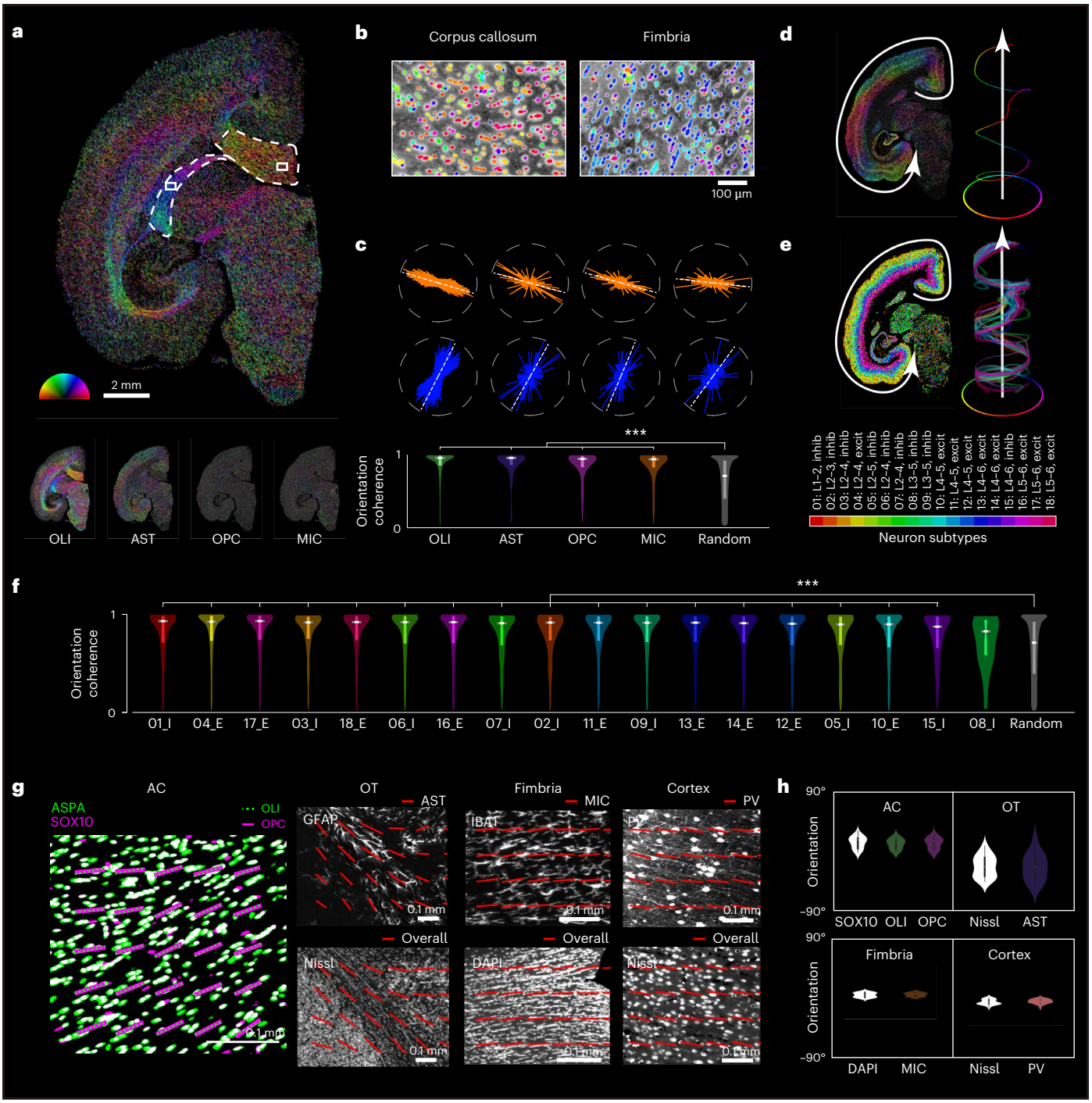

https://doi.org/10.1038/s41592-025-02865-2

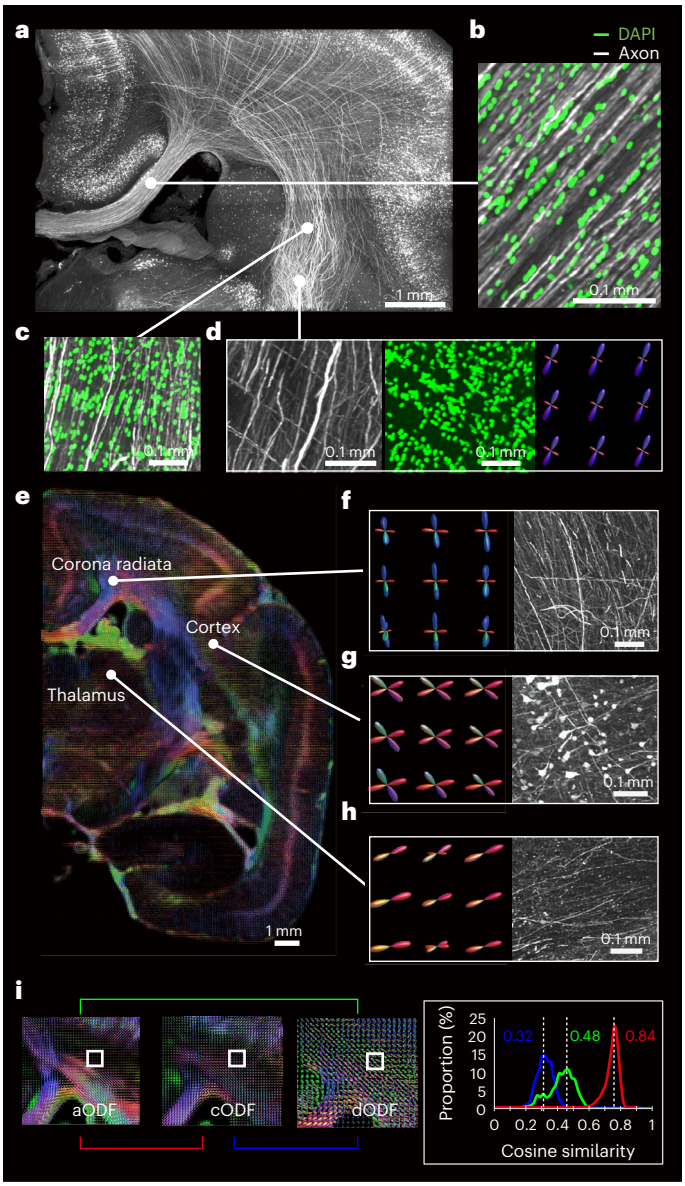

Fig. 3 | Alignment of axonal and cytoarchitectonic orientations revealed by brain-wide neuronal tracing. a, Brain-wide neuronal tracing in the marmoset achieved through systemic virus delivery of AAV.CAP-B10-hSyn-EGFP. **b**–**d**, Alignments between axonal orientation and spatial organization of cells labeled by DAPI staining in various brain structures: the corpus callosum (**b**), the internal capsule regions without (**c**) or with (**d**) fiber intersecting. For the internal capsule region with fiber intersecting, CABLE-derived cODF is also displayed. **e**–**h**, Additional representations of axonal orientations and CABLE-derived ODFs in the corona radiata (**f**), cortex (**g**) and thalamus (**h**). **i**, Comparative analysis of aODFs, cODFs and dODFs. The white square areas in the corona radiata were used for cosine similarity analysis. Red, aODFs versus cODFs; green, aODFs versus dODFs, blue cODFs versus dODFs.

secondary somatosensory cortex (S2) were mainly concentrated laterally, and fibers associated with cortical area 1 (A1) or area 2 (A2) were predominantly concentrated in the intermediate region.

Moreover, the proportion of streamlines terminating in the gyral crowns (A3) versus the walls (A1/A2/PF/S2) in CABLE tractograms was statistically indistinguishable from the virus-labeled ground truth (Fig. 4a,b). In contrast, most tracts generated by dMRI tractography primarily entered A3 (Fig. 4a,b and Supplementary Fig. 15), reflecting a gyral bias[30]. In the macaque brain, we manually delineated the crown and wall regions of a precentral gyrus and compared the distribution of streamline endpoints. CABLE-based streamlines were more evenly distributed across crown and wall regions, while dMRI-based streamlines showed a pronounced bias toward the crown (Supplementary Fig. 16). These results suggest that CABLE tractography more accurately captures fiber turnings and alleviates the gyral bias observed in conventional diffusion-based approaches.

We also evaluated this capability by reconstructing the fiber pathways of the inferior forceps, validated through AAV axon tracing within the same marmoset brain (Fig. 4c–e). The inferior forceps is a relatively obscure commissural tract encircling the posterior hippocampus but not directly connected to it. Initially identified in pioneering neuronal tracing studies in macaques, it bilaterally links the ventral occipital–temporal lobes[32,33]. Despite its potential importance for interhemispheric communication within the ventral visual system, this tract has not been accurately reconstructed using dMRI or other methodologies and is seldom referenced in the literature. By introducing AAV-hSyn-SV40-NLS-Cre and AAV-CAG-DIO-tdTomato-WPRE-hGH-pA viruses into the ventral visual area 4 region of a marmoset, we mapped axon projections using whole-brain VISoR imaging, unveiling the bilateral connections of the inferior forceps between the ventral occipital cortices of both hemispheres (Fig. 4d). Preceding the trajectory toward the inferior forceps, efferent axons traverse two other major fiber bundles—the sagittal stratum and the vertical occipital fasciculus (Fig. 4c). This complex intersection of fibers has led to the failure of dMRI tractography in identifying the correct axon pathway from the cortex to the inferior forceps. In contrast, CABLE-derived cODFs retained the directional component pointing toward the inferior forceps tracts and accurately traced the axonal pathways via tractography (Fig. 4e), showing mirroring of the viral tracing data from the same brain (Fig. 4d). These results underscore the capacity of CABLE in resolving intersecting fiber pathways.

CABLE reveals fiber tract abnormality in a diseased neonatal human brain

The CABLE technique does not rely on transgenic or virus-based labeling, thus presenting an approach for studying fiber tract abnormalities associated with human brain diseases. We acquired volumetric image data from DAPI-stained human brain samples derived from a deceased 19-day-old newborn baby suffering neonatal HIE, a major cause of neonatal morbidity and mortality. We applied CABLE analysis on these samples to obtain 3D cytoarchitectures across various brain regions (Fig. 5). Despite the apparent severe deficiency of hippocampi in this brain sample (Fig. 5a), common among neonates who died of HIE[34], several fiber pathways appeared largely unaffected by the hypoxia. For example, in the internal capsule of this newborn HIE brain, cells were precisely aligned with axonal pathways, yielding cODFs with an inferior-to-superior orientation (Fig. 5b). Similarly, the motor cortex exhibited cytoarchitectonic orientation perpendicular to cortical columns, with adjacent glial cells aligning with the predominant direction of deep white matter, indicating a mature state of cellular organization within motor regions (Fig. 5c).

However, such cytoarchitectonic organization patterns were not consistently presented across all brain regions. For instance, the body of the corpus callosum exhibited neither ellipsoidal soma shapes nor cellular arrangement with commissural fibers (Fig. 5d). Unlike that for the internal capsule, CABLE-derived tractography was unable to obtain continuous streamlines in the corpus callosum due to the chaotic cODF orientations (Fig. 5e), suggesting defective connectivity in the corpus callosum of this newborn HIE brain. To further substantiate this, we examined a mouse hypoxia–ischemia model induced by coagulation of the right common carotid artery. Similar to observations in the human sample, the hypoxia–ischemia mouse exhibited hippocampal injury (Fig. 5f) and a characteristic loss of cytoarchitectonic coherence in the corpus callosum of the affected hemisphere (Fig. 5g–j). These results demonstrate that acute hypoxic–ischemic injury disrupts cytoarchitectonic organization, possibly

https://doi.org/10.1038/s41592-025-02865-2

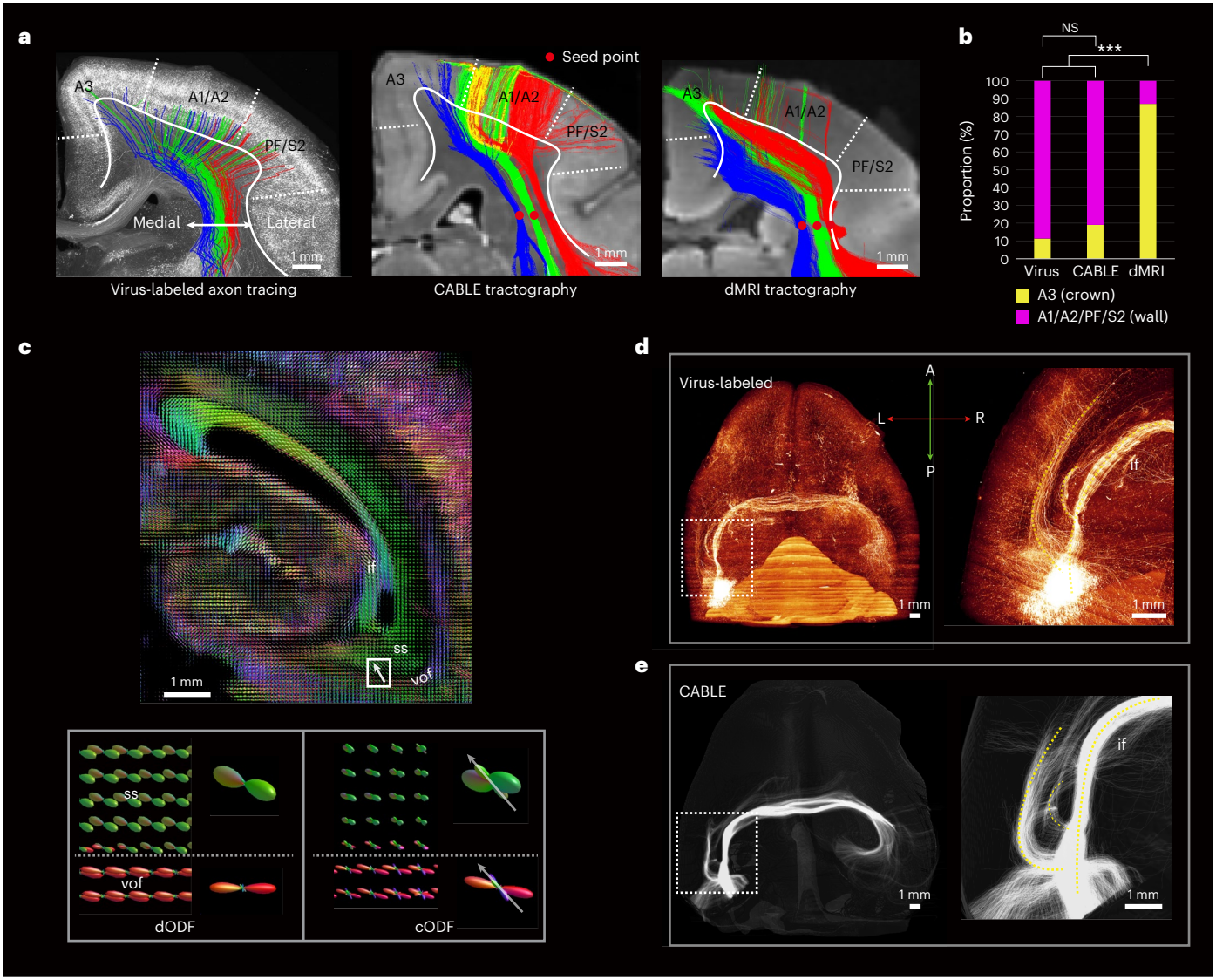

Fig. 4 | Reconstruction of fiber tracts in the marmoset with CABLE tractography. a, Left: a coronal section of brain-wide neuronal tracing in the marmoset brain, with representative single-axon traces annotated in colored tracks. Middle: CABLE-based tractography, with tractography seeds marked by red dots. Right: dMRI-based tractography. White solid lines indicate the gray–white matter boundaries, and dotted lines denote the boundaries of different cortical areas. PF, parietal area PF; S2, secondary somatosensory cortex; A1–3, cortical areas 1–3. **b**, The proportion of virus-labeled axons (crown/wall = 15/117), CABLE-derived (crown/wall = 38/162) and dMRI-derived (crown/wall = 174/26) tractography streamlines entering the crown and wall regions. NS, not significant ($P = 0.09$); ***$P = 1.4 \times 10^{-41}$ (dMRI-virus) and $P = 1.1 \times 10^{-41}$ (dMRI-CABLE); chi-squared test (two sided). **c**, Visualization of dODF and cDOF in the same marmoset brain. cODF map (upper) around the occipital lobe and zoomed-in views (lower) of the area indicated by the white box, visualizing both the dODFs and cODFs. The cODFs estimate the fiber orientations toward the inferior forceps (indicated by arrows), passing through the vertical occipital fasciculus (vof) and the sagittal stratum (ss). **d**, AAV virus injection in the left ventral occipital area (dotted boxed area; enlarged on the right) reveals axons navigating through the vertical occipital fasciculus and sagittal stratum, entering the inferior forceps (if) and terminating in the right ventral occipital area. **e**, CABLE-based tractography, initiated from the virus injection sites, reconstructed the axon tracts visualized in **d**.

due to widespread apoptosis. Nevertheless, this case illustrates that the CABLE method can be applied to large-scale human brain samples and may be used to detect tract abnormalities associated with neurological diseases.

Discussion

While our study was conducted using the VISoR imaging platform[16] and focused on specific tissue types and stainings, the method can be potentially adapted to other imaging modalities and tissue preparations[35–37]. Leveraging the intrinsic anisotropy of individual cells, CABLE achieves spatial and angular resolutions approaching the cellular scale, constrained primarily by the size (typically 5–20 µm) and fractional anisotropy (typically below 0.6) of single cells.

The CABLE method is based on the alignment observed between cytoarchitectonic orientation and axon fiber orientation. The mechanism underlying this alignment represents an interesting subject for future research. A few studies have shown that oligodendrocytes were arranged in orderly rows in certain white matter structures of rodents, enabling the analysis of white matter fiber architecture using structure tensor analysis on 2D Nissl-stained sections[10,18]. We propose that the observed cytoarchitectonic orientation coherence across diverse cell types arises from a combination of mutual spatial constraints and developmental mechanisms. Gradients of biochemical signals regulate cell proliferation, differentiation, migration and axon guidance during development[38,39]. In parallel, biomechanical forces—such as axonal tension along the radial axis and compressive pressure from

https://doi.org/10.1038/s41592-025-02865-2

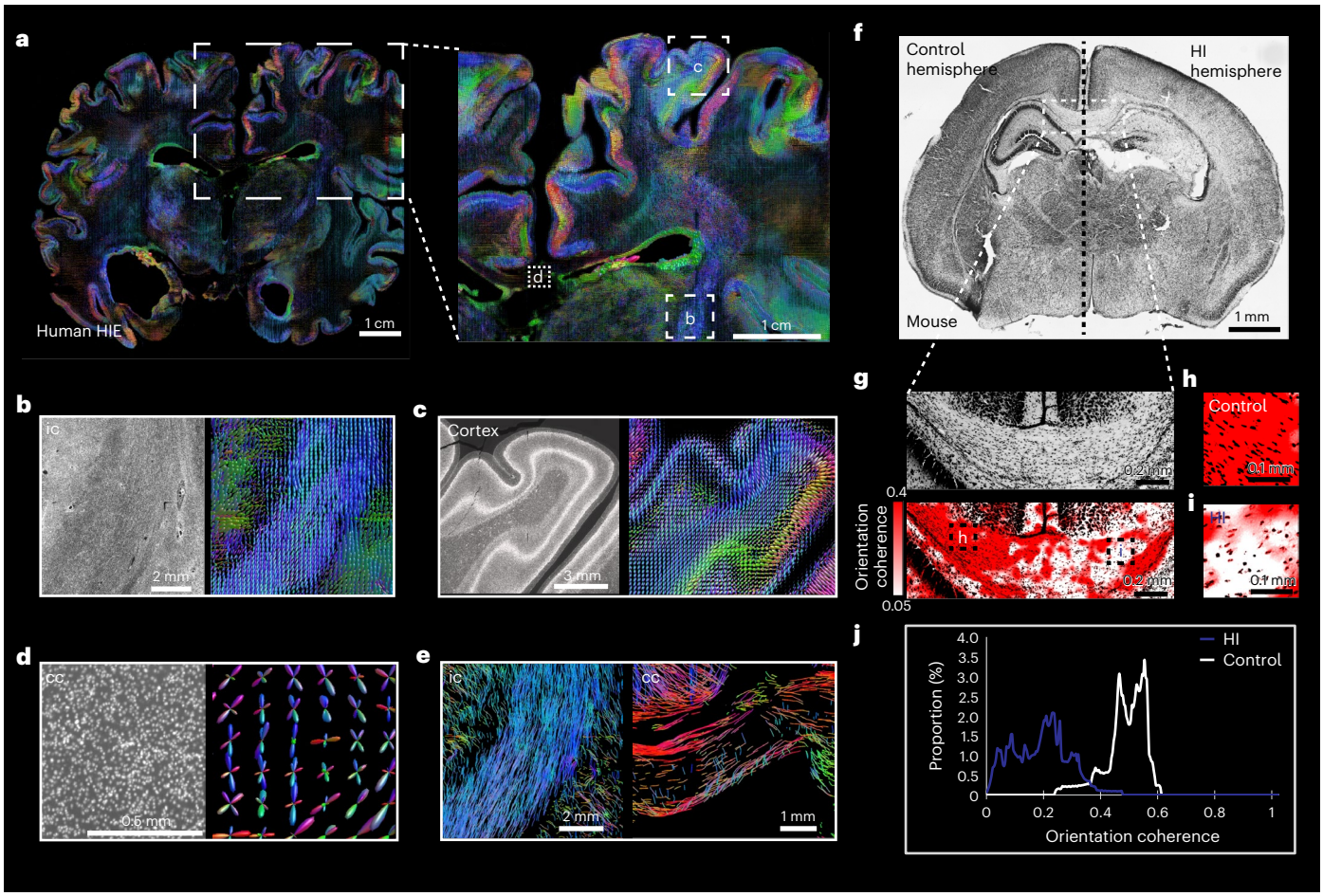

Fig. 5 | Application of CABLE to the diseased newborn human brain. **a**, Illustration of fiber orientation in a newborn human brain analyzed by CABLE. Left: a coronal section of the brain showing 3D cODFs. Right: a zoomed-in view of the area annotated by the dashed rectangle. **b**–**d**, Zoomed-in views of the areas marked in **a**, including the internal capsule (**b**), the neocortex (**c**) and the corpus callosum (**d**). Left: raw fluorescence Nissl-stained images. Right: 3D cODFs estimated by CABLE. **e**, CABLE-based tractography at the internal capsule (left) and the corpus callosum (right), using random seed points. **f**, A coronal section of a hypoxia–ischemia (HI) mouse modeled with right common carotid arterial coagulation. **g**, Top: enlarged view of the corpus callosum area indicated by the rectangle in **f**. Bottom: structure tensor coherence map, where redder hues indicate higher coherence. **h**,**i**, Enlarged views of the dashed box areas in **g**. **j**, Comparison between control areas (**h**) and HI-affected areas (**i**), showing a significant difference in orientation coherence (two-sided Mann–Whitney *U*-test, $P < 1 \times 10^{-300}$, $n = 78{,}120$ sliding windows).

tightly wrapping myelin sheaths[40,41]—may impose mechanical constraints on neighboring cells, influencing their soma shape and spatial arrangement. These biomechanical factors are also associated with the tension-based theory of cortical morphogenesis[42,43]. Together, these chemical and mechanical cues likely contribute to the emergence of coherent cellular anisotropy. Analogous to how urban structures co-develop through mutual constraints, the brain's cytoarchitectonic organization may result from reciprocal interactions among neurons, glia and axons.

While in general all cell types we examined displayed high orientation coherence, there were differences among cell types exhibiting coherence of different levels. The relatively high orientation coherence found in the two *Vip*-expressing GABAergic neuronal subtypes of layers I and II aligns with previous reports of their role in cross-layer disinhibition, which is associated with their bipolar elongated morphology and projections into deeper layers[44]. The two *Rorb*-expressing glutamatergic subtypes in layer IV and layer V showed relatively low orientation coherence, possibly due to the presence of layer IV spiny stellate neurons, which receive long-range thalamic inputs and participate in local circuits[45]. While there is an organizational trend for orienting all brain cells, subtle cell-type-specific differences in cytoarchitectonic orientation exist and may be associated with the functional roles of these cells.

CABLE offers a flexible framework for fiber tract reconstruction, with adaptability across both experimental and algorithmic dimensions. On the experimental side, CABLE leverages intrinsic cytoarchitectonic features across general cell types, eliminating the need for transgenic models or virus-based labeling. Algorithmically, CABLE extracts local directional information from image data and applies spherical deconvolution to resolve disentangled fiber orientations. This directional information can be derived from a range of sources, such as image gradients at multiple spatial scales (capturing both single-cell shapes and multicellular tissue organization), ellipsoid-based cell fitting using long axes or structure tensor analysis. The internal representation of the DSDF or ODF is also tunable, allowing for higher angular resolution through denser directional sampling and higher-order spherical harmonics. We anticipate that future algorithmic advances will further enhance the precision of CABLE.

Taken together, these flexibilities make CABLE a powerful and extensible platform for brain-wide fiber mapping across species and imaging platforms, including applications in human brain disorders such as HIE. Previous dMRI work has demonstrated structural changes in the white matter associated with psychiatric brain disorders including schizophrenia, bipolar disorder, autism spectrum disorder, major depressive disorder and epilepsy[46,47]. The high-resolution 3D imaging and CABLE analysis could be applied to postmortem brains and surgical

samples, for elucidating fine-grained abnormal connectivity underlying brain dysfunction associated with these diseases.

Finally, although the CABLE method could achieve accurate estimates of the fiber tract directions and is particularly effective in resolving intersecting and bending fibers, it is unable to reconstruct the full trajectories of individual axons, which often feature complex turns and bifurcations. At present, these fine-scale trajectories can only be visualized through single-axon tracing with sparse viral labeling[16,48]. Such data will be valuable for establishing ground truth and guiding future improvements of CABLE tractography toward comprehensive and precise mapping of primate and human brain connectivity. It should also be noted that, for high-precision mapping of whole brains, the processing and analysis of the extensive datasets generated by whole-brain volumetric imaging at cellular resolution pose extreme computational challenges[49]. For example, the size of multichannel data from an adult macaque brain generated in this study reached 1 petabyte, and that of an adult human brain would be larger than 5 petabytes, exceeding that of the largest human brain image dataset H01 (ref. 50). These challenges necessitate the development of more efficient data processing algorithms and open data sharing platforms. International collaboration will facilitate progress in constructing a comprehensive atlas of human brain cytoarchitecture and connectivity at the cellular resolution.

Online content

Any methods, additional references, Nature Portfolio reporting summaries, source data, extended data, supplementary information, acknowledgements, peer review information; details of author contributions and competing interests; and statements of data and code availability are available at https://doi.org/10.1038/s41592-025-02865-2.

References

1. Fields, R. D. White matter in learning, cognition and psychiatric disorders. *Trends Neurosci.* **31**, 361–370 (2008).
2. Liu, C. et al. A resource for the detailed 3D mapping of white matter pathways in the marmoset brain. *Nat. Neurosci.* **23**, 271–280 (2020).
3. Bihan, D. L. Looking into the functional architecture of the brain with diffusion MRI. *Nat. Rev. Neurosci.* **4**, 469–480 (2003).
4. Jeurissen, B., Descoteaux, M., Mori, S. & Leemans, A. Diffusion MRI fiber tractography of the brain. *NMR Biomed.* **32**, e3785 (2019).
5. Larsen, L., Griffin, L. D., GRäßel, D., Witte, O. W. & Axer, H. Polarized light imaging of white matter architecture. *Microsc. Res. Tech.* **70**, 851–863 (2007).
6. Basser, P. J., Mattiello, J. & Bihan, D. L. MR diffusion tensor spectroscopy and imaging. *Biophys. J.* **66**, 259–267 (1994).
7. Tuch, D. S. Q-ball imaging. *Magn. Reson. Med.* **52**, 1358–1372 (2004).
8. Wedeen, V. J. et al. The geometric structure of the brain fiber pathways. *Science* **335**, 1628–1634 (2012).
9. Axer, M. et al. Estimating fiber orientation distribution functions in 3D-polarized light imaging. *Front. Neuroanat.* **10**, 40 (2016).
10. Schurr, R. & Mezer, A. A. The glial framework reveals white-matter fiber architecture in human and primate brains. *Science* **374**, 762–767 (2021).
11. Hayashi, T. et al. The nonhuman primate neuroimaging and neuroanatomy project. *NeuroImage* **229**, 117726 (2021).
12. Lin, M. K. et al. A high-throughput neurohistological pipeline for brain-wide mesoscale connectivity mapping of the common marmoset. *eLife* **8**, e40042 (2019).
13. Yan, M. et al. Mapping brain-wide excitatory projectome of primate prefrontal cortex at submicron resolution and comparison with diffusion tractography. *eLife* **11**, e72534 (2022).
14. Bullock, D. N. et al. A taxonomy of the brain's white matter: twenty-one major tracts for the 21st century. *Cereb. Cortex* **32**, 4524–4548 (2022).
15. Wang, H. et al. Scalable volumetric imaging for ultrahigh-speed brain mapping at synaptic resolution. *Natl Sci. Rev.* **6**, 982–992 (2019).
16. Xu, F. et al. High-throughput mapping of a whole rhesus monkey brain at micrometer resolution. *Nat. Biotechnol.* **39**, 1521–1528 (2021).
17. Chen, A. et al. Spatiotemporal transcriptomic atlas of mouse organogenesis using DNA nanoball-patterned arrays. *Cell* **185**, 1777–1792 (2022).
18. Suzuki, M. & Raisman, G. The glial framework of central white matter tracts: Segmented rows of contiguous interfascicular oligodendrocytes and solitary astrocytes give rise to a continuous meshwork of transverse and longitudinal processes in the adult rat fimbria. *Glia* **6**, 222–235 (1992).
19. Andersson, M. et al. Axon morphology is modulated by the local environment and impacts the noninvasive investigation of its structure–function relationship. *Proc. Natl Acad. Sci. USA* **117**, 33649–33659 (2020).
20. Schmahmann, J. D. & Pandya, D. N. *Fiber Pathways of the Brain* (Oxford Univ. Press, 2006).
21. Tournier, J.-D., Calamante, F., Gadian, D. G. & Connelly, A. Direct estimation of the fiber orientation density function from diffusion-weighted MRI data using spherical deconvolution. *NeuroImage* **23**, 1176–1185 (2004).
22. Anderson, A. W. Measurement of fiber orientation distributions using high angular resolution diffusion imaging. *Magn. Reson. Med.* **54**, 1194–1206 (2005).
23. Szczupak, D. et al. Direct interhemispheric cortical communication via thalamic commissures: a new white-matter pathway in the rodent brain. *Cereb. Cortex* **31**, 4642–4651 (2021).
24. Reveley, C. et al. Diffusion MRI anisotropy in the cerebral cortex is determined by unmyelinated tissue features. *Nat. Commun.* **13**, 6702 (2022).
25. Lin, J. -P. et al. Transcriptomic architecture of nuclei in the marmoset CNS. *Nat. Commun.* **13**, 5531 (2022).
26. Kleshchevnikov, V. et al. Cell2location maps fine-grained cell types in spatial transcriptomics. *Nat. Biotechnol.* **40**, 661–671 (2022).
27. Goertsen, D. et al. AAV capsid variants with brain-wide transgene expression and decreased liver targeting after intravenous delivery in mouse and marmoset. *Nat. Neurosci.* **25**, 106–115 (2022).
28. Ieva, A. D., Fathalla, H., Cusimano, M. D. & Tschabitscher, M. The indusium griseum and the longitudinal striae of the corpus callosum. *Cortex* **62**, 34–40 (2015).
29. Thomas, C. et al. Anatomical accuracy of brain connections derived from diffusion MRI tractography is inherently limited. *Proc. Natl Acad. Sci. USA* **111**, 16574–16579 (2014).
30. Reveley, C. et al. Superficial white matter fiber systems impede detection of long-range cortical connections in diffusion MR tractography. *Proc. Natl Acad. Sci. USA* **112**, E2820–E2828 (2015).
31. Tournier, J. -D. et al. MRtrix3: a fast, flexible and open software framework for medical image processing and visualisation. *NeuroImage* **202**, 116137 (2019).
32. Demeter, S., Rosene, D. L. & van Hoesen, G. W. Interhemispheric pathways of the hippocampal formation, presubiculum, and entorhinal and posterior parahippocampal cortices in the rhesus monkey: the structure and organization of the hippocampal commissures. *J. Comp. Neurol.* **233**, 30–47 (1985).
33. Demeter, S., Rosene, D. L. & Hoesen, G. W. V. Fields of origin and pathways of the interhemispheric commissures in the temporal lobe of macaques. *J. Comp. Neurol.* **302**, 29–53 (1990).
34. Schiering, I. A. M. et al. Correlation between clinical and histologic findings in the human neonatal hippocampus after perinatal asphyxia. *J. Neuropathol. Exp. Neurol.* **73**, 324–334 (2014).

35. Seiriki, K. et al. High-speed and scalable whole-brain imaging in rodents and primates. *Neuron* **94**, 1085–1100 (2017).
36. Zhou, C. et al. Continuous subcellular resolution three-dimensional imaging on intact macaque brain. *Sci. Bull.* **67**, 85–96 (2022).
37. Park, J. et al. Integrated platform for multiscale molecular imaging and phenotyping of the human brain. *Science* **384**, eadh9979 (2024).
38. Luo, L. Architectures of neuronal circuits. *Science* **373**, eabg7285 (2021).
39. Dickson, B. J. Molecular mechanisms of axon guidance. *Science* **298**, 1959–1964 (2002).
40. Chicurel, M. E., Chen, C. S. & Ingber, D. E. Cellular control lies in the balance of forces. *Curr. Opin. Cell Biol.* **10**, 232–239 (1998).
41. Fletcher, D. A. & Mullins, R. D. Cell mechanics and the cytoskeleton. *Nature* **463**, 485–492 (2010).
42. Essen, D. C. V. A tension-based theory of morphogenesis and compact wiring in the central nervous system. *Nature* **385**, 313–318 (1997).
43. Essen, D. C. V. A 2020 view of tension-based cortical morphogenesis. *Proc. Natl Acad. Sci. USA* **117**, 32868–32879 (2020).
44. Apicella, A. J. & Marchionni, I. VIP-expressing GABAergic neurons: disinhibitory vs. inhibitory motif and its role in communication across neocortical areas. *Front. Cell. Neurosci.* **16**, 811484 (2022).
45. Freitag, F. B., Ahemaiti, A., Weman, H. M., Ambroz, K. & Lagerström, M. C. Targeting barrel field spiny stellate cells using a vesicular monoaminergic transporter 2-Cre mouse line. *Sci. Rep.* **11**, 3239 (2021).
46. Koshiyama, D. et al. White matter microstructural alterations across four major psychiatric disorders: mega-analysis study in 2937 individuals. *Mol. Psychiatry* **25**, 883–895 (2020).
47. Hatton, S. N. et al. White matter abnormalities across different epilepsy syndromes in adults: an ENIGMA-Epilepsy study. *Brain* **143**, 2454–2473 (2020).
48. Li, S. et al. Single-neuron reconstruction of the macaque primary motor cortex reveals the diversity of neuronal morphology. *Neurosci. Bull.* **41**, 525–530 (2024).
49. Shen, Y. et al. Mapping big brains at subcellular resolution in the era of big data in zoology. *Zool. Res.* **43**, 597–599 (2022).
50. Shapson-Coe, A. et al. A petavoxel fragment of human cerebral cortex reconstructed at nanoscale resolution. *Science* **384**, eadk4858 (2024).

Methods

Ethics statement

This study complies with all relevant ethical regulations. Ethical approval for the use of human and animal samples was obtained from the relevant institutional review boards and ethics committees, as detailed in the following section.

Brain sample acquisition

Primate whole-brain sample IDs and related figures are listed in Supplementary Table 1.

Macaque brains. Three adult, 10-year-old, male rhesus macaques (*Macaca mulatta*) were used in this study. Macaques were obtained from the breeding colonies of the Primate Research Center of Kunming Institute of Zoology, Chinese Academy of Sciences (KIZ, CAS), which was accredited by the Association for Assessment and Accreditation of Laboratory Animal Care (AAALAC International). The experimental procedures were approved by the Institutional Animal Care and Use Committee (IACUC) of KIZ, CAS (IACUC number IACUC18018).

For perfusion, 4% hydrogel monomer solution (HMS) was prepared by mixing acrylamide (4% final concentration; V900845, Sigma), bisacrylamide (0.05% final concentration; V3141, Promega), 10× phosphate-buffered saline (PBS; 1× final concentration; 70011044, Thermo Fisher), paraformaldehyde (PFA; 4% final concentration; 157-8, Electron Microscopy Sciences), distilled water and VA-044 thermal initiator (0.25% final concentration; 223-02112, Wako). Macaques were deeply anesthetized by 10 mg per kg body weight ketamine hydrochloride injection (intramuscular (i.m.), 50 mg ml^{-1}, Zhong Mu Bei Kang pharmaceutical industry limited company, China) and maintained with 20 mg per kg body weight pentobarbital sodium (i.m., 40 mg ml^{-1}; Merck). Transcardial perfusions were carried out 30 min after anesthesia, by sequentially perfusing with the following solutions at the specified speeds: PBS 8 l (37 °C, 10 ml s^{-1}), PBS 1 l (4 °C, 1.5 ml s^{-1}), 4% HMS 1 l (4 °C, 1.5 ml s^{-1}) and 4% HMS 1 l (4 °C, 0.3 ml s^{-1}). The brains were extracted immediately after perfusion within 30 min.

Human brain. Brain tissue (HS001) of a male newborn, and a human brain tissue block from epilepsy surgery were obtained from the National Health and Disease Human Brain Tissue Resource Center, Anhui Medical University (NBC-AMU) following permission for a brain autopsy and the use of brain material and clinical data for research purposes. Informed consent for autopsy and the use of body material was approved by the parents. Clinical details were given by the NBC-AMU. The experimental procedures were approved by the Anhui Provincial Children's Hospital Medical Research Ethics Committee (number EYLL-2024-048).

Marmoset brains. Six common marmosets (*Callithrix jacchus*) were used in this study. CJ001, a 3-year-old male marmoset, was used to obtain coronal sections for Stereo-seq. CJ003, a 3-year-old male marmoset, was used to obtain sagittal sections for Stereo-seq as biological replication. CJ002, a 5-year-old female marmoset, was used for hippocampus interhemispheric projection labeling. CJ004, a 7.5-year-old male marmoset, was used for viral labeling across the blood–brain barrier. CJ005 was a newborn marmoset, used for white matter development analysis. Both VISoR and dMRI imaging data were acquired from three marmoset brains (CJ002, CJ004, CJ005). CJ006, a 3.5-year-old female marmoset, was used for immunofluorescence staining. The animal studies and procedures were approved (ION-2019011) by the Animal Care and Use Committee of the Center for Excellence in Brain Science & Intelligence Technology (CEBSIT), Chinese Academy of Sciences, Shanghai, China. Marmosets were individually housed under conditions that adhered to institutional guidelines of CEBSIT, with a 12-h light–dark cycle (lights on from 7:00 to 19:00), a humidity- and temperature-controlled environment (27 °C to 30 °C) and ad libitum access to food and water.

For CJ001 and CJ003, animals were induced into anesthesia through the administration of a combination of tiletamine hydrochloride and zolazepam hydrochloride (i.m., 25 mg per kg body weight) and xylazine hydrochloride (i.m., 20 mg per kg body weight). Following induction, the brain underwent immediate perfusion with room-temperature artificial cerebrospinal fluid saturated with 95% oxygen and 5% carbon dioxide, succeeded by 4 °C artificial cerebrospinal fluid perfusion at a rate of 100 ml min^{-1}.

For animals CJ002, CJ004, CJ005 and CJ006, anesthesia was induced and maintained with 1.5% isoflurane in 100% oxygen. Transcardial perfusion was then performed using the following solutions and flow rates:

(1) For CJ002, CJ004 and CJ005: 500 ml of PBS (4 °C, 30 ml min^{-1}), followed by 100 ml of 4% HMS (4 °C, 40 ml min^{-1}), 250 ml of 4% HMS (4 °C, 30 ml min^{-1}) and 1 l of 4% HMS (4 °C, 20 ml min^{-1}).
(2) For CJ006: 500 ml of PBS (4 °C, 30 ml min^{-1}), followed by 100 ml of 4% PFA (4 °C, 40 ml min^{-1}), 250 ml of 4% PFA (4 °C, 30 ml min^{-1}) and 1 l of 4% PFA (4 °C, 20 ml min^{-1}).

Marmoset brains were extracted immediately following perfusion, within 30 min.

Mouse brains. All mouse experiments were approved by the Institutional Animal Care and Use Committee at the Shenzhen Institutes of Advanced Technology (SIAT), Chinese Academy of Sciences (SIAT-IACUC-231110-NS-XF-A2358). The mice were housed under a 12-h light–dark cycle and had free access to food and water.

Neonatal hypoxia–ischemia mouse models were used to mimic the neonatal human HIE[51–53]. Pregnant C57BL/6J mice at gestational day 17 were purchased from VITAL RIVER Laboratories (Guangzhou). The day of birth was defined as postnatal day 0. On postnatal day 3, male mouse pups were subjected to hypoxia–ischemia insult. The pups were anesthetized with isoflurane, and the right common carotid artery was coagulated and severed using an electric cautery pen. The entire surgical procedure was completed within 5–10 min. After a 1-h recovery period, the pups were placed in a hypoxic chamber at 37 °C with a gas mixture of 8% oxygen and 92% nitrogen for 75 min. The pups were then returned to their cages until they were euthanized on postnatal day 7 (P7), then the mice were deeply anesthetized and perfused with 4% PFA (30535-89-4, Aladdin). For conventional histological study, brains were collected and post-fixed in 4% PFA. After 30% sucrose incubation for 48 h, the brains were sectioned at a thickness of 50-µm with a cryostat (CM1950, Leica). Coronal sections were then stained with a Nissl dye (cresyl violet; 10510-54-0, Coolaber) and photographed with a research slide scanner (VS200, Olympus).

For immunostaining, 4-month-old male C57BL/6J mice were anesthetized via intraperitoneal injection of a ketamine–xylazine mixture (10 mg per kg body weight ketamine hydrochloride, 50 mg ml^{-1}, Zhong Mu Bei Kang; 1 mg per kg body weight xylazine hydrochloride, 50 mg ml^{-1}, Jilin Hua Mu). Transcardial perfusion was then performed sequentially with 30 ml of PBS (37 °C, 10 ml min^{-1}), 30 ml of PBS (4 °C, 10 ml min^{-1}) and 30 ml of 4% PFA (4 °C, 10 ml min^{-1}). Brains were extracted after perfusion and temporarily stored in 4% PFA.

For vasculature labeling, 4-month-old male C57BL/6J mice were anesthetized with 1.5% isoflurane and injected retro-orbitally with 75 µl of *Lycopersicon esculentum* lectin conjugated to DyLight 488 (L32470, Thermo Fisher) or DyLight 649 (DL-1178-1, Vector Labs). One hour after injection, secondary anesthesia was administered, followed by transcardial perfusion with the following solutions in sequence: 30 ml of PBS (37 °C, 10 ml min^{-1}), 30 ml of PBS (4 °C, 10 ml min^{-1}), 30 ml of 4% PFA (4 °C, 10 ml min^{-1}) and 75 µl of lectin dissolved in 30 ml of ice-cold PBS (4 °C, 3 ml min^{-1}). Brains were extracted immediately after perfusion and stored temporarily in 4% PFA.

Datasets

Macaque PLI dataset. The PLI data used in this study are part of the BigMac Dataset[54,55], an open-access resource combining in vivo MRI, extensive postmortem MRI and multi-contrast microscopy for multimodal characterization of a single, whole macaque brain. In this dataset, all slices were coronal sections with adjacent slices spaced 350 µm apart at a resolution of 4 µm. In addition, the dataset includes microscopic data stained with Gallyas silver, details of which can be found at https://open.win.ox.ac.uk/pages/amyh/bigmacdocumentation/.

Macaque dMRI dataset. The macaque dMRI data used in this study were obtained from a previously published study[30]. This dMRI dataset was acquired ex vivo using a 7-T horizontal Bruker scanner, with each brain specimen scanned for over 61 h. The resulting dMRI data have an isotropic spatial resolution of 250 µm.

Viral labeling

Whole-brain viral labeling. For marmoset CJ004, deep anesthesia was induced by 1.5% isoflurane inhalation before surgery. The injection of 2 ml of the tracer (AAV.Cap-B10, (ssAAV-hSyn-EGFP-WPREs-SV40pA), 1×10^{13} genome copies per ml) was performed by tail vein injection. The virus tracer was also used for mice (100 µl; 1:10,000 dilution) via retro-orbital vein injection after anesthesia was induced with 1.5% isoflurane. Animals were euthanized 8 weeks after the injection for brain collection.

Specific circuit labeling. For marmoset CJ002, deep anesthesia was induced by 1.5% isoflurane inhalation before surgery. A stereotaxic apparatus was used for fixing the head of the marmoset, and the cranial perforation surgery was performed using a dental drill while core temperature and heart rate were monitored. Marmoset CJ002 was injected with a recombinant AAV (rAAV) mixture (AAV2/9, (rAAV-hSyn-SV40-NLS-Cre) 1:10,000, (rAAV-CAG-DIO-tdTomato) 1:4; 1,000 nl) into the occipital region (ventral visual area 4) of the left hemisphere (anteroposterior, −3.79 mm; mediolateral, 6.79 mm; dorsoventral, 9.75 mm). The viral solution was injected at the rate of ~200 nl min^{-1}. Antibiotics were used for the following 3 days after the surgery. Macaque RM008 was injected with a mixture of AAV-Cre and AAV-DIO-EGFP (1:1) into the mediodorsal nucleus of the thalamus. Eight weeks after the surgery, the marmoset and the macaque were euthanized for brain collection. Injection sites were further confirmed from reconstructed whole-brain images.

SMART brain mapping

Whole-brain volumetric imaging data of rodent and primate brains were acquired following the SMART brain mapping pipeline[16], including preprocessing (post-fixation processes), serial sectioning, tissue clearing and optional staining, VISoR2 volumetric microscopy, semiautomated whole-brain reconstruction and optional fiber tracing. A step-by-step protocol of this full pipeline has been deposited in the protocols.io repository[56].

Post-fixation processes. For standard samples, the brains were immersed in 4% HMS and stored at 4 °C for 2–7 days, depending on brain size and tissue density (typically 2 days for mouse brains; 7 days for primate brains). Following fixation, samples were transferred to an embedding solution consisting of a 1:1 mixture of 4% HMS and 20% bovine serum albumin (BSA; final concentrations: 2% HMS and 10% BSA; V900933, Sigma). Brains were incubated in the embedding solution for 0.5–7 days, again depending on tissue size and density. Embedding was completed by polymerization at 37 °C for 4–5 h, after which samples were washed three times in PBS to remove residual reagents.

For samples intended for immunolabeling, the brains were post-fixed in 4% PFA instead of 4% HMS and embedded in a 10% fish skin gelatin solution (10% final concentration in PBS; K91420, KEHBIO). The gelatin was then solidified by immersion in 4% PFA. These modifications were designed to improve antibody penetration efficiency.

Sectioning. All embedded brain samples were sectioned into 300-µm-thick slices. Whole marmoset brains were sectioned using a vibroslicer (Compresstome VF-800, Precisionary Instruments), yielding approximately 70–105 slices per brain. Slices from each brain were distributed across three six-well cell culture plates, with 3–5 slices and 10 ml of PBS per well, and stored at 4 °C. Whole macaque brains were also sectioned using the Compresstome VF-800, generating approximately 200–250 slices per brain. For the whole newborn human brain sample, sectioning into 300-µm-thick slices was performed using a custom-designed vibraslicer[57]. Mouse brains and small human brain tissue blocks were sectioned using a vibroslicer (Compresstome VF-700, Precisionary Instruments), yielding approximately 40–50 slices per sample. These were placed in 12-well cell culture plates. Each slice was marked with a notch on the left ventral side of the embedding block to preserve orientation for whole-brain reconstruction.

Slice clearing. The 300-µm-thick brain slices were cleared using the two-step PuClear method[16]. In the first step, slices were incubated in 5% Triton X-100 (T9284, Sigma) in PBS (PuClear solution A) at 37 °C with gentle shaking for 1–4 days to enhance membrane permeability (1 day for mouse brains; 4 days for primate brains). Slices could optionally undergo immunostaining following this step. Before imaging, slices were mounted on glass substrates and incubated in a refractive index-matching solution to increase optical transparency. This solution (PuClear solution B) was prepared by mixing 50 wt% iohexol (29242990.99, Hisyn Pharmaceutical), 23 wt% urea (A600148-0002, Sangon), 11 wt% 2,2′,2″-nitrilotriethanol (V900257, Sigma) and 16 wt% distilled water, yielding a final refractive index of 1.52. Brain slices were incubated in PuClear solution B for 6–12 h at room temperature with gentle shaking before imaging.

Staining. Staining was performed following membrane permeabilization with PuClear solution A. General staining targeted the cell nuclei and/or somal Nissl bodies for later CABLE analysis. Brain slices were incubated with DAPI (C1006, Beyotime Biotechnology; used undiluted) for 1 day to label nuclei, and with NeuroTrace 640/660 deep-red fluorescent Nissl stain (NT640; N21483, Thermo Fisher) to label the somato morphology. For primate brain slices, NeuroTrace was diluted at a ratio of 1:100 and applied for 4 days; for mouse brain slices, it was diluted at a ratio of 1:200 and applied for 2 days. All slices were subsequently washed three times with PBS.

For immunolabeling, permeabilized slices were transferred to cell culture plates or Petri dishes based on tissue size and incubated in a blocking solution containing 0.5 M glycine (68898, Sigma) and 0.3% Tween-20 (T104863, Aladdin) in PBS (0.3% PBST) for 4 h at 37 °C with gentle shaking. This was followed by a 1-h wash in PBS at room temperature. Samples were then incubated with primary antibodies diluted in 0.3% PBST for 2–4 days at 4 °C with gentle shaking, followed by three washes in 0.3% PBST. Secondary antibody incubation was performed under the same conditions for an additional 2–4 days, also followed by three washes. General DAPI and NeuroTrace (Nissl) staining was performed after immunofluorescence labeling.

The source and amount/dilution of primary and secondary antibodies used in this study are listed in Supplementary Tables 2 and 3, respectively.

VISoR2 microscopy. Cleared brain slices were imaged using the VISoR2 technique[16] on commercial imaging systems (VISoR M1, Bitelligen). 10×/0.3-NA objectives equipped in these systems were used to generate raw images of the slices at $1 \times 1 \times 2.5\text{-}\mu m^3$ pixel resolution. Roughly, dual-channel imaging of a rhesus macaque brain generated 500 TB of raw images. These images were compressed and transferred

to a computing cluster for analysis. Triple-channel imaging of a marmoset brain generated 20 TB of images after compression, with an approximate compression ratio of 8:1.

Whole-brain reconstruction. Volume stitching of VISoR2 raw images was performed with custom codes (https://github.com/SMART-pipeline/Volume-reconstruction/). As described previously[16], this procedure included intra-slice stitching, multichannel registration, inter-slice stitching and global optimization. For practical use, downsampled reconstructed image datasets of whole brains at 4 × 4 × 4-μm^3 resolution were generated, and the deformation fields between the raw images and the reconstructed brain were stored and used as required to generate the highest-resolution (1 × 1 × 1-μm^3) images of the regions of interest for specific analyses.

Semiautomated tracing. Single-axon reconstruction of the virus-labeled marmoset brain (CJ004) was performed in a semiautomated manner with the Lychnis software (https://github.com/SMART-pipeline/Lychnis-tracing/)[16], or the NeuroFly tool (https://github.com/beanli161514/NeuroFly/)[58], a plugin of the open-source software napari[59]. Each axon segment was initially reconstructed by a human annotator, followed by dual-round proofreading by two other independent annotators.

dMRI meso-scale connectivity mapping

Acquisition of ex vivo dMRI data of marmosets. The brain sample of marmoset CJ004 was scanned using a 3D diffusion-weighted multi-shot spin-echo echo planar imaging sequence on a 9.4 T/12-cm MRI (Bruker Biospin), equipped with a 35-mm birdcage volume coil. The acquisition parameters were set as follows: repetition time = 165 ms; echo time = 23.44 ms; number of segments = 24; field of view = 26.4 × 34.2 × 19.2 mm^3; and matrix size = 176 × 168 × 128, resulting in a 150-μm isotropic spatial resolution. In total, 96 diffusion-weighted images (DWIs) were collected, comprising 6 at b = 0 s mm^{-2}, 60 at b = 1,500 s mm^{-2} and 30 at b = 3,000 s mm^{-2}.

Preprocessing of dMRI data and diffusion tractography. The dMRI data were first denoised using the 'dwidenoise' function of MRtrix3 (ref. 31) to extract noise-only principal components from a large number of DWIs. This greatly improved the signal-to-noise ratio of the final image contrasts[60]. Then, the data were eddy-corrected using the eddy_correct function in FSL[61] and were fitted with the DTI model and multi-shell multi-tissue constrained spherical deconvolution using DTIFIT in FSL and MRtrix3, respectively. These fittings generated contrast images such as fractional anisotropy and dODF (also referred to as 'orientation density function' or 'fiber orientation distribution function' in the literature) with principal fiber direction information (DEC). The dODF was used for probabilistic tractography using the 'tckgen' function of MRtrix3.

Spatial transcriptomics

Tissue collection for Stereo-seq. After perfusion, the marmoset brain was divided in half using a stereotaxic micromanipulator (SMM-200, Narishige), and the left hemisphere tissue samples were mixed with 4 °C optimal cutting temperature compound (4583, Sakura), quickly frozen on dry ice into tissue blocks, and stored at −80 °C. The above procedure was completed within 30 min to minimize RNA degradation. Diethyl pyrocarbonate-treated sterilized water (B501005-0005, Sangon Biotech) was used for solutions and equipment cleaning.

Tissue cryo-sectioning was conducted at −20 °C using pre-cooled tools (for example, chips, forceps) to obtain multiple coronal (for CJ001) or sagittal (for CJ003) sections with a predetermined 10-μm thickness and gap. After cryo-sectioning, each tissue section was flattened on a −20 °C metal plane of the cryo-section platform in a dry environment and then placed on a pre-cooled Stereo-seq chip progressively to prevent air bubbles and tissue folding.

Library preparation and sequencing. The brain tissue of interest was sampled via Stereo-seq capture chips (1 cm × 2 cm; BGI Research). Initially, the chips were cleansed with Nuclease-Free H_2O supplemented with 0.05 U μl^{-1} RNase inhibitor (M0314L, NEB) and air-dried. Then, tissue sections measuring 10 μm in thickness were affixed to the Stereo-seq capture chips' surface and incubated at 37 °C for 3 min. Subsequently, the chips and the tissue sections were fixed in pre-cooled methanol at −20 °C for 40 min. The chips were treated with 100 μl of tissue fluorescence staining solution at room temperature for 5 min, which comprised 0.1× SSC solution (AM9770, Thermo), 1:200 dilution of nucleic acid dye (Q10212, Thermo Fisher) and 2 U μl^{-1} RNase inhibitor. The chips were washed with wash buffer (0.1× SSC supplemented with 2 U μl^{-1} RNase inhibitor) and dried using a Power dust remover (M-6318, MATIN) at room temperature. Finally, 5 μl of glycerin was carefully applied to the center of each tissue section to avoid bubbles. Imaging was conducted using a Motic Custom PA53 FS6 microscope, and the chips were covered with a cover glass before in situ capture at the channel of FITC (10× objective).

After the washing step, tissue sections placed on the capture chip were permeabilized using a solution containing 0.1% pepsin (P7000, Sigma) in 0.01 M HCl buffer at 37 °C for 6 min. The RNA liberated from the permeabilized tissue was then captured by the DNA nanoball (DNB) and reverse transcribed for 2 h at 42 °C using a 100 μl RT mix containing 10 U μl^{-1} reverse transcriptase (18064-014, Invitrogen), 1 mM dNTPs, 1 M betaine solution PCR reagent, 7.5 mM $MgCl_2$, 5 mM dithiothreitol, 2 U μl^{-1} RNase inhibitor, 2.5 μM Stereo-seq-TSO (5-CTGCTGACGTACTGAGAGGC/rG//rG//iXNA_G/-3) and 1× first-strand buffer. After reverse transcription, tissue sections were washed twice with wash buffer and then subjected to digestion with tissue removal buffer (10 mM Tris-HCl, 25 mM EDTA, 100 mM NaCl, 0.5% SDS) at 37 °C for 30 min. The chips were treated with Exonuclease I (M0293L, NEB) at 37 °C for 1 h. The resulting first-strand cDNAs were amplified using KAPA HiFi Hotstart Ready Mix (KK2602, Roche) with 0.8 μM of the cDNA-PCR primer (5-CTGCTGACGTACTGAGAGGC-3).

PCR reactions were performed by incubating the mixture at 95 °C for 5 min, followed by 15 cycles at 98 °C for 20 s, 58 °C for 20 s, 72 °C for 3 min, and a final incubation at 72 °C for 5 min. The resulting PCR products were purified using VAHTS DNA Clean Beads (N411-03, Vazyme, ×0.6) and quantified using the Qubit™ dsDNA Assay Kit (Q32854, Thermo Fisher). To fragment the products, 20 ng underwent in-house Tn5 transposase treatment at 55 °C for 10 min, after which the reactions were stopped with 0.02% SDS and incubated at room temperature for 5 min. The fragmented products were then amplified using 1× KAPA HiFi Hotstart Ready Mix and 0.3 μM of both the Stereo-seq-Library-F primer (/5phos/CTGCTGACGTACTGAGAGGCA-3) and the Stereo-seq-Library-R primer (5-GAGACGTTCTCGACTCAGCAGA-3). The reaction consisted of one cycle of 95 °C for 5 min, 13 cycles of 98 °C for 20 s, 58 °C for 20 s and 72 °C for 30 s, followed by one cycle of 72 °C for 5 min. Purification of the PCR products was achieved using VAHTSTM DNA Clean Beads (×0.6 and ×0.15). The resulting library was sequenced at the China National Gene Bank using an MGI DNBSEQ-Tx sequencer. Read 1 was 35 bp in length, and read 2 was 100 bp.

Preprocessing and cell-type annotation of Stereo-seq dataset. The Stereo-seq Analysis Workflow (SAW, https://github.com/BGIResearch/SAW/) was used to process the sequencing data and generate a gene-to-spot matrix for two coronal sections and one sagittal section. For later CABLE analysis of these sections, cell segmentation was implemented using a deep-learning-based segmentation method, Cellpose[62,63], applied to digital images of ssDNA staining sections. The gene-to-spot matrix of each section was aggregated to create a cell-by-gene matrix, which was then used to generate 'AnnData' objects using the Scanpy package in Python[64].

Identification of cell types using DestVI. The DestVI deep-learning method was utilized to map cell types, which were clustered and identified from an existing snRNA-seq dataset, CjPCA[25], onto the spatial transcriptome datasets. Before cell-type annotation, all aggregated 'AnnData' objects were merged, and genes shared between the Stereo-seq dataset and the snRNA-seq dataset were determined. To identify glial cell types, including OPCs, in the spatial transcriptomic (Stereo-seq) dataset, we used DestVI[65], a deep-learning-based method for deconvolving spatial data using reference single-cell RNA-seq information. Specifically, we transferred cell-type annotations from a previously published snRNA-seq dataset[25] by first training a single-cell latent variable model (LVM) on the reference dataset. The decoder from this model was then used to initialize a spatial LVM, which we trained on our merged Stereo-seq dataset. This approach enabled us to estimate, for each spatially resolved cell, the probability of it belonging to a given annotated cell type.

The spatial mapping model was trained to learn the basis of gene expression from the top 4,000 highly variable genes in the snRNA-seq dataset, with 300 training epochs. Subsequently, the probabilities of six cell types, including neurons, oligodendrocytes, OPCs, astrocytes, microglia and vascular/meningeal/ventricular cells, were transferred from the snRNA-seq dataset to each spatial transcriptome section, with 2,500 training epochs per section.

Stringent criteria were adopted to determine the exact cell type for each cell. These criteria included ensuring that the probability of the first choice exceeded 0.6, the difference between the probability of the first choice and that of the second choice exceeded 0.4, and in the space produced by the uniform manifold approximation and projection algorithm[66], the annotated cell type was locally homogeneous. This was implemented by ensuring that more than 75% of the nearest neighbors of a cell in the uniform manifold approximation and projection space belonged to the same cell type.

The neuron subclusters identified in CjPCA were not utilized for further annotation of neurons in the spatial transcriptome due to its limited sampling in the cortex. Instead, we adopted another snRNA-seq dataset[67], which provided detailed categorizations for cortical excitatory and inhibitory neurons. Eighteen neuron subclusters were mapped to the spatial transcriptome dataset using DestVI, as described previously. The parameters chosen for this mapping included 500 training epochs for a single-cell LVM and 3,000 training epochs for a spatial LVM, allowing for a more comprehensive learning of neuron categories in the models.

CABLE analysis of spatial transcriptome brain sections

Orientation coherence analysis on Stereo-seq sections. After extracting cellular contours with Cellpose, the orientation θ of each cell was estimated as the orientation of the major axis of the least-square-fitted ellipse[68]. For each cell, a cytoarchitectonic orientation θ_{local} was defined as the median orientation angle of all other cells within a 100-µm radius, excluding the cell itself. Subsequently, the orientation coherence for each cell was defined as the cosine similarity between θ and θ_{local}, which equals to $\cos(\theta - \theta_{\text{local}})$. This measurement reflects the degree of alignment between a cell's orientation and the cytoarchitectonic orientation of its surrounding local environment. To assess whether the observed levels of orientation coherence in our data are significantly different from what would be expected by chance, we constructed a null model by randomizing the orientation of each cell while preserving its spatial location. The randomization was performed by sampling from a continuous uniform distribution ranging from 0 to π. After each randomization, we calculated the orientation coherence distribution of all cells. This process was repeated 5,000 times to generate an averaged simulated distribution of the orientation coherence. The distribution generated from the null model simulation was then compared to the real data. The two-sided Mann–Whitney *U*-test was used to determine whether the observed distribution was the same as the generated distribution. A *P* value below 0.05 was considered statistically significant, indicating that the observed orientation coherence is unlikely to have occurred by chance.

Cortical coordinate mapping with Laplace's equation. Neuron subclusters mapped by DestVI exhibited distinct layer distributions. To describe their layer positions, we applied Laplace's equation to the delineated cortical contours to generate nonoverlapping, nominally parallel-running radial streamlines that intersected the boundary contours orthogonally and tangential streamlines that were almost parallel to the pial surface[69]. Cells were mapped to a radial–tangential coordinate system based on its relative position on the radial and tangential streamlines that passed through it.

Then we divided the neocortex into canonical cortical layers based on neurons' radial position distribution. The median value of radial positions of the outermost subcluster was designated as the position of layer II, while that of the innermost subcluster was designated as the position of layer VI. The peak position of the neuron radial position distribution was designated as the position of layer IV. Positions of layers III and V were then determined through linear interpolation. Subsequently, the layers of each neuron subcluster were annotated based on the nearest layers to the 25th percentile and 75th percentile of radial positions of neurons within that subcluster.

CABLE analysis of 3D images

Designing the CABLE framework for high-resolution orientation extraction and fiber tracing. The Nissl-ST method developed by Schurr and Mezer[10] extracts fiber orientation from the spatial arrangement of glial cells in 2D sections using structure tensor analysis. Inspired by this approach, we aimed to develop algorithms capable of recovering local neuronal fiber orientations from cytoarchitecture, without relying on fiber-specific labeling.

Their method uses structure tensor analysis[70,71], which estimates the dominant orientation in a local region by identifying the eigenvector associated with the smallest eigenvalue of the structure tensor. In essence, this corresponds to performing a local principal component analysis (PCA) of the image gradients. While these gradients already contain directional cues, PCA is limited in its ability to resolve multiple overlapping fiber orientations. Consequently, while the method performs well in regions with a single dominant orientation, such as the corpus callosum, it may fail to accurately resolve crossing fibers commonly found in broader white matter regions[72], capturing only the primary orientation or even yielding incorrect directions (Extended Data Fig. 2).

In our high-resolution 3D images, we observed that nuclei and somata exhibit locally coherent anisotropic shapes. This single-cell-level directional information provides higher spatial resolution than cellular arrangement alone and was later shown to be critical for accurately recovering multiple fiber orientations (Supplementary Fig. 3). Our approach begins by directly computing per-voxel gradients from high-resolution images, capturing subtle morphological features such as nuclear and somatic shape.

Importantly, these image gradients share a key anisotropic property with diffusion-weighted MRI signals: both exhibit stronger signals perpendicular to the fiber direction and weaker signals along it. This analogy enables us to adopt and adapt processing pipelines from dMRI. In our framework, we define a DSDF that pools the directional information from image gradients within a local analysis window, conceptually analogous to the dMRI signal. The resulting fiber orientation distribution can then be estimated through spherical deconvolution methods[21,22], which are well established in dMRI analysis.

To implement the above approach, we define the local DSDF $\text{DSDF}_v(\theta, \phi)$, in polar coordinates as an estimation of the spherical gradient density surrounding a given voxel v of image I. A peaked spherical kernel function (PSF) is used as a smoothing kernel to approximate the

density distribution from discrete gradient samples, analogous to a kernel density estimator for reconstructing a probability density function from a finite set of data points. More specifically, the gradients of all voxels within the neighborhood of v are treated as directed delta functions and convolved with the PSF to yield a continuous directional density estimate as given by equation (1):

$$\mathrm{DSDF}_v(\theta,\phi) = \frac{1}{N}\sum_{v'\in I,\mathrm{dist}(v,v')<r/2}(||\nabla I(v')||_2 \cdot \delta_{S^2}(\nabla I(v')) \times \mathrm{PSF}(\theta,\phi)),\ \forall v \in I \tag{1}$$

where $\nabla I(v') \in \mathbb{R}^3$ is the image gradient at position v'; $\delta_{S^2}(\nabla I(v'))$ is the Dirac delta function defined on the unit sphere S^2, pointing in the direction of $\nabla I(v')$; an asterisk denotes the convolution operation on the sphere; 'dist' defines the local analysis window (a cube) centered at v with size r; $\|\cdot\|_2$ represents the Euclidean norm; $N = |\{v' \in I|\mathrm{dist}(v,v') < r/2\}|$ is a normalization factor equal to the number of voxels within the analysis window.

The PSF is defined in equation (2):

$$\mathrm{PSF}(\theta,\phi) = \langle \vec{u}(\theta,\phi), \vec{u}(0,0)\rangle^n \tag{2}$$

where $\langle\cdot,\cdot\rangle$ denotes the inner product, and $\vec{u}(\theta,\phi) \in \mathbb{R}^3$ is the unit vector pointing in the direction of spherical coordinate θ,ϕ, and n is an even integer.

Thus, the DSDF of each pooled voxel (with pooling size r) is represented as a set of amplitudes of uniformly distributed directions $\vec{d}$ on the unit sphere S^2 as given by equation (3):

$$\mathrm{DSDF}_v(\vec{d_j}) = \frac{1}{N}\sum_{v'\in I,\mathrm{dist}(v,v')<\frac{r}{2}}||\nabla I(v')||_2 \cdot \left\langle \frac{\nabla I(v')}{||\nabla I(v')||_2}, \vec{d_j}\right\rangle^n, v \in I, j \in 1\ldots m \tag{3}$$

where $\vec{d}_j = \vec{u}(\theta_j,\phi_j)$ for $j = 1\ldots m$. Notably, the formulation of DSDF voxels mirrors that of DWI voxels, enabling direct analogies in downstream analysis.

Note that the aggregated gradients (represented here as the DSDF) near a given location result from a linear mixture of the gradients from each nearby cell or nucleus. In other words, a convolutional relationship exists: the standard gradient distribution of a unidirectional bundle, convolved with the fiber bundle direction distribution (cODF), produces the DSDF. Therefore, applying spherical deconvolution to the DSDF yields the cODF. We get equation (4):

$$\mathrm{DSDF}_v(\theta,\phi) = \mathrm{cODF}_v(\theta,\phi) \times R(\theta,\phi) \tag{4}$$

The response function $R(\theta,\phi)$ is the gradient distribution of unidirectional fibers. This is similar to dMRI analysis. In the dMRI spherical deconvolution analysis model, it assumes that the dMRI signal $S'(\theta,\phi)$ results from the convolution of the response function $R'(\theta,\phi)$ with the fiber ODF dODF, as shown in equation (5):

$$S'_v(\theta,\phi) = \mathrm{dODF}_v(\theta,\phi) \times R'(\theta,\phi) \tag{5}$$

where $R'(\theta,\phi)$ is assumed to be symmetric around ϕ, and is normally measured from a unidirectional fiber region (usually the corpus callosum). At any given location, $\mathrm{dODF}(\theta,\phi)$ can be derived by spherical deconvolution from S'[73].

Similarly, the cytoarchitectonic ODF can be derived from the DSDF by spherical deconvolution. Fiber pathways can then be reconstructed using tractography algorithms based on the cODFs[4].

Based on assumption that the main source of cytoarchitectonic orientation originates from the anisotropy of individual cells, the theoretical angular resolution is determined by experimentally observed cellular anisotropy, which is 0.6 (the 90th percentile measured in the marmoset corpus callosum), given an angular resolution of approximately 26.3° (Supplementary Note 1). This empirical value gives us references for parameter selection during the implementation of CABLE.

Implementing CABLE based on MRtrix3. Since CABLE and dMRI spherical deconvolution share the same mathematical model, we used the well-established tool MRtrix3 for implementing CABLE in our fluorescence image datasets.

The n number in equation (2) is set to 100 to create continuous distribution without loss of angular resolution (Supplementary Note 1).

For computing the DSDF given by equation (3), predefined unit vectors $\vec{d}_j = \vec{u}(\theta_j,\phi_j)$ for $j = 1\ldots m$ were generated using the 'dirgen' function in MRtrix3. We set $m = 45$, which satisfies the required angular sampling density based on the theoretical angular resolution derived from cellular anisotropy (Supplementary Note 1).

Considering that the volume size of primate brain images is too large (a macaque brain dataset acquired at $1\times1\times2.5$-μm^3 resolution with VISoR2/SMART pipeline is approximately 250 TB), we first downsampled the raw images to $4\times4\times4$-μm^3 voxel resolution, which still maintains the cellular anisotropy. To further accelerate the computation, we sampled the gradient at every second voxel in each dimension while calculating the DSDF. For computational efficiency, in this study, we set the size of analysis window r to be 80 μm for marmosets and rhesus monkeys and 160 μm for the newborn human.

Before calculating the final ODF, the DSDF is smoothed with a Gaussian kernel, computed using the 'mrfilter' command in MRtrix3. The kernel size is kept below the analysis window size r, and as small as possible to preserve sharp transitions (for example, between brain areas), while improving tractography robustness. More advanced methods such as local PCA denoising could also be used[74,75].

The response function $R(\theta,\phi)$ is estimated by manually selecting the DSDFs at the corpus callosum and expressed in terms of spherical harmonics using the 'dwi2response' function of MRtrix3. For spherical deconvolution, we apply modern constrained variants such as CSD[76] and MSMT-CSD[77] to DSDFs to get more robust results. Although our data are single shell, MSMT-CSD provides stronger non-negativity constraints than CSD and thus yields cleaner and more reliable orientation estimates in practice. We therefore used MSMT-CSD for its practical advantages, even though the full capabilities of the multi-shell, multi-tissue model were not utilized. The maximum spherical harmonics order $l_{\max}$ in MSMT-CSD is empirically chosen as 8 to 12 unless specified otherwise, based on the practical performance and computation efficiency (Supplementary Note 1).

The deconvolved ODFs are represented in the spherical harmonic series format recognized by the MRtrix3 command 'tckgen', which we utilize for tractography. When necessary, asymmetrical filtering of ODFs can be applied to assess specific neuronal pathways[78], as supported within the CABLE pipeline.

In this research, we set the maximum tracking distance to 100 mm (that is, unlimited length) and the limiting amplitude to 0.1 times the peak of corpus callosum ODF as the reference. This helps limit tracking interruptions due to sharp changes in direction and reduces instances where tracking extends outside the brain. All streamlines were reconstructed using MRtrix3's iFOD1 or iFOD2 algorithms[79–81], using fourth-order Runge–Kutta integration (rk4, for iFOD1) or high power values (≥2, for iFOD2) to constrain randomness, unless otherwise stated. These settings reduce random angular deviation and produce more deterministic-like behavior while still leveraging the directional information embedded in the ODF shape. We set the maximum angle between successive steps to the default 15° (iFOD1) or 45° (iFOD2), and the step to the default 0.5 voxel (iFOD2) or 0.25 voxel (iFOD1).

Comparison of CABLE and structure tensor-based analysis. To compare the results of our method with classical 3D structure tensor analysis

(Extended Data Fig. 2), we calculate the distribution of the structure tensor directions on a sliding block of 80-μm scale. Each eigenvector corresponding to the smallest eigenvalue of the structure tensor is computed within a 16-μm window, and the eigenvectors within each 80-μm block will be convolved with a 12th order apodised point spread function[82] to get an ODF of 80-μm size.

Comparison of different tractography configurations. To compare fibers reconstructed using the CABLE method with virus-labeled fibers (Fig. 4a and Supplementary Fig. 15), the seeds are placed near the virus-labeled sites, and their start directions are set to match the directions of the virus-labeled axons at the corresponding position (Fig. 4e).

CABLE-derived peak orientation map. To extract the peak orientation of the cODF for visualization (Fig. 1e), we compute the peak orientation map of the cODF using the Mrtrix3 command 'fod2fixel'.

CABLE analysis for 2D images

In 2D images, we used structure tensor as the image feature that represents cytoarchitectonic orientation.

To visualize the directionality of cell rows and soma morphology (Fig. 1b), we compute structure tensor in 2D cross-sectional images. For the cell rows, σ (the smooth window size) and ρ (the local neighborhood window size) are set to 8 μm and 80 μm, respectively. For the cell morphology, we first segment each cell using Cellpose and then compute the structure tensor separately with $\sigma = 0$ and ρ equal to the diameter of each cell. The results of structure tensor analysis are represented by colored lines or by marking colors directly on the cells, using the same coloring rules as for the 3D orientation, namely red for left–right direction, blue for inferior–superior direction and green for anterior–posterior direction.

To compare the cytoarchitectonic orientation coherence in different regions, we calculated the local coherence from the images within each local window using OrientationJ[83,84] plugins in Fiji[85], and the σ and ρ are set to 10 μm and 40 μm to 80 μm respectively. The coherence C is a value ranging from 0 and 1 derived from the eigenvalues (λ) of the structure tensor[86]: $C = (\lambda_{max} - \lambda_{min}) / (\lambda_{max} + \lambda_{min})$. Higher coherence indicates more focused orientation within the window.

Reporting summary

Further information on research design is available in the Nature Portfolio Reporting Summary linked to this article.

Data availability

The complete image datasets for macaque, marmoset, human and mouse brains exceed 300 TB in total size and are therefore impractical to upload in full to a public data repository. A subset of the data is available at https://cable.bigconnectome.org, including: demo datasets for testing the CABLE analysis code; a representative slice image of the macaque brain (RM009) used in Fig. 1c; the Stereo-seq dataset analyzed in Fig. 2, Extended Data Figs. 5 and 6 and Supplementary Figs. 9–11; and a multimodal marmoset brain dataset (CJ004) used in Figs. 3 and 4. Additional datasets related to any figure or video in this work are available from the corresponding author upon reasonable request, using feasible data transfer methods such as physical hard drives, cloud storage or on-site access.

Code availability

The code and installation guide for CABLE analysis can be found at the GitHub repository (https://github.com/BrainCABLE) under the MIT License. A frozen version of the code has been archived on Zenodo (https://doi.org/10.5281/zenodo.17092643)[87]. A step-by-step protocol for using CABLE analysis in various datasets has been deposited on the protocols.io repository[88].

References

51. Brancaccio, P. Preconditioning in hypoxic-ischemic neonate mice triggers Na^+ –Ca^{2+} exchanger-dependent neurogenesis. *Cell Death Discov.* **8**, 318 (2022).
52. Rumajogee, P., Bregman, T., Miller, S. P., Yager, J. Y. & Fehlings, M. G. Rodent hypoxia–ischemia models for cerebral palsy research: a systematic review. *Front. Neurol.* **7**, 57 (2016).
53. Vannucci, S. J. & Back, S. A. The Vannucci model of hypoxic-ischemic injury in the neonatal rodent: 40 years later. *Dev. Neurosci.* **44**, 186–193 (2022).
54. Howard, A. F. D. et al. An open resource combining multi-contrast MRI and microscopy in the macaque brain. *Nat. Commun.* **14**, 4320 (2023).
55. Tendler, B. C. et al. The Digital Brain Bank, an open access platform for post-mortem imaging datasets. *eLife* **11**, e73153 (2022).
56. Hu, X., Shen, Y., Yang, Y., Bi, G. -Q. & Xu, F. SMART brain mapping. *protocols.io* https://doi.org/10.17504/protocols.io.36wgq658klk5 (2025).
57. Ma, C. et al. High precision vibration sectioning for 3D imaging of the whole central nervous system. *J. Neurosci. Methods* **399**, 109966 (2023).
58. Zhao, R. et al. NeuroFly: a framework for whole-brain single neuron reconstruction. Preprint at https://arxiv.org/abs/2411.04715 (2024).
59. Sofroniew, N. et al. napari: a multi-dimensional image viewer for Python. *Zenodo* https://doi.org/10.5281/zenodo.15193038 (2025).
60. Cordero-Grande, L., Christiaens, D., Hutter, J., Price, A. N. & Hajnal, J. V. Complex diffusion-weighted image estimation via matrix recovery under general noise models. *NeuroImage* **200**, 391–404 (2019).
61. Andersson, J. L. R. & Sotiropoulos, S. N. An integrated approach to correction for off-resonance effects and subject movement in diffusion MR imaging. *NeuroImage* **125**, 1063–1078 (2016).
62. Stringer, C., Wang, T., Michaelos, M. & Pachitariu, M. Cellpose: a generalist algorithm for cellular segmentation. *Nat. Methods* **18**, 100–106 (2021).
63. Pachitariu, M. & Stringer, C. Cellpose 2.0: how to train your own model. *Nat. Methods* **19**, 1634–1641 (2022).
64. Wolf, F. A., Angerer, P. & Theis, F. J. SCANPY: large-scale single-cell gene expression data analysis. *Genome Biol.* **19**, 15 (2018).
65. Lopez, R. et al. DestVI identifies continuums of cell types in spatial transcriptomics data. *Nat. Biotechnol.* **40**, 1360–1369 (2022).
66. McInnes, L., Healy, J. & Melville, J. UMAP: uniform manifold approximation and projection for dimension reduction. Preprint at https://arxiv.org/abs/1802.03426 (2018).
67. Krienen, F. M. et al. A marmoset brain cell census reveals regional specialization of cellular identities. *Sci. Adv.* **9**, eadk3986 (2023).
68. Fitzgibbon, A., Pilu, M. & Fisher, R. B. Direct least square fitting of ellipses. *IEEE Trans. Pattern Anal. Mach. Intell.* **21**, 476–480 (1999).
69. Adamson, C. L. et al. Thickness profile generation for the corpus callosum using Laplace's equation. *Hum. Brain Mapp.* **32**, 2131–2140 (2011).
70. Bigun, J. *Optimal Orientation Detection of Linear Symmetry*. In *Proc. IEEE-First International Conference on Computer Vision* 433–438 (IEEE, 1987).
71. Jähne, B. *Spatio-Temporal Image Processing: Theory and Scientific Applications* (Springer, 1993).
72. Jeurissen, B., Leemans, A., Tournier, J., Jones, D. K. & Sijbers, J. Investigating the prevalence of complex fiber configurations in white matter tissue with diffusion magnetic resonance imaging. *Hum. Brain Mapp.* **34**, 2747–2766 (2013).
73. Dell'Acqua, F. & Tournier, J. D. Modelling white matter with spherical deconvolution: how and why? *NMR Biomed.* **32**, e3945 (2019).

74. Koay, C. G. & Basser, P. J. Analytically exact correction scheme for signal extraction from noisy magnitude MR signals. *J. Magn. Reson.* **179**, 317–322 (2006).
75. Manjón, J. V. et al. Diffusion weighted image denoising using overcomplete local PCA. *PLoS ONE* **8**, e73021 (2013).
76. Tournier, J. -D., Calamante, F. & Connelly, A. Robust determination of the fibre orientation distribution in diffusion MRI: non-negativity constrained super-resolved spherical deconvolution. *NeuroImage* **35**, 1459–1472 (2007).
77. Jeurissen, B., Tournier, J. -D., Dhollander, T., Connelly, A. & Sijbers, J. Multi-tissue constrained spherical deconvolution for improved analysis of multi-shell diffusion MRI data. *NeuroImage* **103**, 411–426 (2014).
78. Karayumak, S. C., Özarslan, E. & Unal, G. Asymmetric orientation distribution functions (AODFs) revealing intravoxel geometry in diffusion MRI. *Magn. Reson. Imaging* **49**, 145–158 (2018).
79. Basser, P. J., Pajevic, S., Pierpaoli, C., Duda, J. & Aldroubi, A. In vivo fiber tractography using DT-MRI data. *Magn. Reson. Med.* **44**, 625–632 (2000).
80. Tournier, J.-D., Calamante, F. & Connelly, A. Improved probabilistic streamlines tractography by 2nd order integration over fibre orientation distributions. In *Proc. 18th Annual Meeting of the International Society for Magnetic Resonance in Medicine* 1670 (2010).
81. Tournier, J., Calamante, F. & Connelly, A. MRtrix: diffusion tractography in crossing fiber regions. *Int. J. Imaging Syst. Technol.* **22**, 53–66 (2012).
82. Raffelt, D., Tournier, J., Crozier, S., Connelly, A. & Salvado, O. Reorientation of fiber orientation distributions using apodized point spread functions. *Magn. Reson. Med.* **67**, 844–855 (2012).
83. Fonck, E. et al. Effect of aging on elastin functionality in human cerebral arteries. *Stroke* **40**, 2552–2556 (2009).
84. Püspöki, Z., Storath, M., Sage, D. & Unser, M. in *Focus on Bio-Image Informatics* (eds De Vos, W. H. et al.) 69–93 (Springer, 2016).
85. Schindelin, J. et al. Fiji: an open-source platform for biological-image analysis. *Nat. Methods* **9**, 676–682 (2012).
86. Rezakhaniha, R. et al. Experimental investigation of collagen waviness and orientation in the arterial adventitia using confocal laser scanning microscopy. *Biomech. Model. Mechanobiol.* **11**, 461–473 (2012).
87. Zhang, Y. & Xiao, Y. Euyz/CABLE: CABLE v.1.0. *Zenodo* https://doi.org/10.5281/zenodo.17092643 (2025).
88. Zhang, Y. et al. Brain CABLE analysis. *protocols.io* https://doi.org/10.17504/protocols.io.5qpvoo5zdv4o (2025).

Acknowledgements

We thank X. Qi, C. Liu, S. Li, X. Zou, R. Li, Y. Cai and F. Wu for experimental support; L. Ding, Z. Yi and H. Xia for software and computing resources maintenance; C. Xu, G. Wang and J. Xi for help with viral injections; and S. Chen for valuable suggestions on the paper. We thank the Single Cell Typing Platform and Non-human Primate Anatomical Research Platform of CEBSIT for assisting with marmoset transcriptomic data collection; thank the 9.4T MRI core facility of CEBSIT for assistance in the MRI imaging; and thank the Marmoset Animal Facility of CEBSIT for animal care. This work was supported by the STI 2030-Major Projects (2022ZD0205200 to F.X. and Y.X.; 2025ZD0219300 and 2022ZD0205000 to C.L.; 2021ZD0200104 to P.-M.L.), Shenzhen Science and Technology Program (RCYX20210706092100003 to F.X.), Shenzhen Medical Research Funds grant (A2303005 to F.X.), National Natural Science Foundation of China grants (32171088 and 32427802 to C.L.; T2522040 to F.X.), a Youth Innovation Promotion Association CAS grant (2022367 to F.X.) and the National Key R&D Program of China (2022YEF0203200 to G.-Q.B.).

Author contributions

Conceptualization: F.X., C.L. and Y.X.; Formal analysis: Y.Z. and T.S.; Funding acquisition: F.X., C.L., Y.X., P.-M.L. and G.-Q.B.; Investigation: Y.S. (acquisition of VISoR data of macaque and human brains), Y.Y. (acquisition of VISoR data of marmoset brains), Xiaowei Hu (immunostaining and mouse HIE data acquisition), L.T., C.J. (mouse HIE model), C.-Y.Y. (prototype of structure tensor analysis), H.W. (human brain sample preparation), X.W., H.L. and H.Y. (viral labeling of marmoset brain); Methodology: Y.Z., T.S. and C.-Y.Y.; Project administration: F.X. and C.L.; Resources: J.-N.Z., H.H., X.W. (human brain samples) and Xintian Hu (macaque brains); Software: C.-Y.Y., R.Z., W.W., Y.L. and P.Z.; Supervision: F.X., C.L., Y.X. and G.-Q.B.; Writing—original draft: C.L., F.X., Y.Z. and T.S.; Writing—review and editing: C.L., F.X., Y.Z., T.S., Y.X. and M.-M.P.

Competing interests

The authors declare no competing interests.

Additional information

Extended data is available for this paper at https://doi.org/10.1038/s41592-025-02865-2.

Supplementary information The online version contains supplementary material available at https://doi.org/10.1038/s41592-025-02865-2.

Correspondence and requests for materials should be addressed to Guo-Qiang Bi, Yanyang Xiao, Cirong Liu or Fang Xu.

Peer review information *Nature Methods* thanks the anonymous reviewers for their contribution to the peer review of this work. Peer reviewer reports are available. Primary Handling Editor: Nina Vogt, in collaboration with the *Nature Methods* team.

https://doi.org/10.1038/s41592-025-02865-2

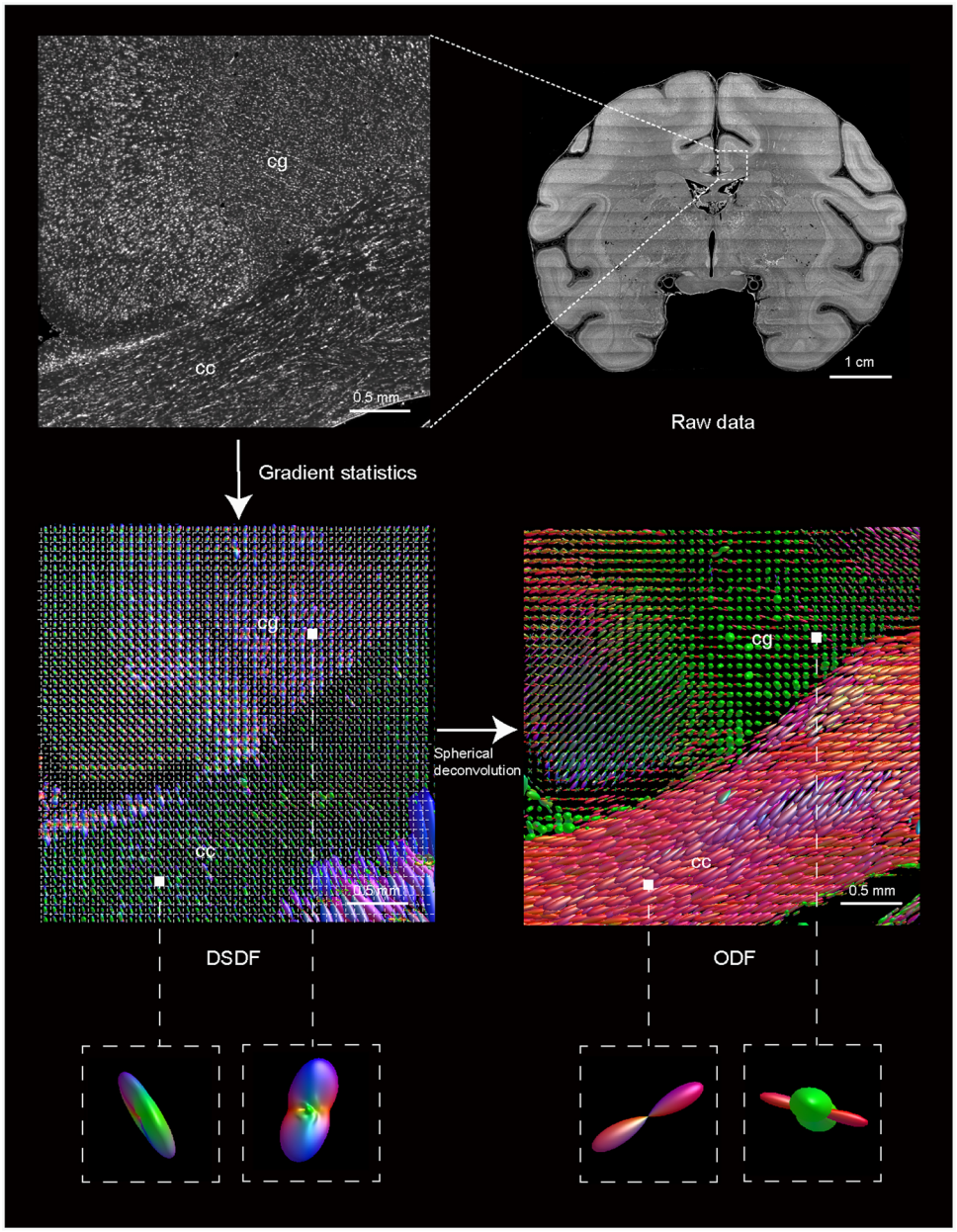

Extended Data Fig. 1 | ODF calculation with CABLE analysis. CABLE extracts local image gradients from each pixel in the cytoarchitectonic image to construct the directional scattering density function (DSDF). Gradients within a local analysis window (illustrated by a grid cell) are aggregated into a single DSDF voxel. Spherical deconvolution is then applied to the DSDF to generate orientation distribution functions (ODF), which recover underlying fiber orientations in both unidirectional (for example, corpus callosum, cc) and crossing (for example, cingulum, cg) fiber regions.

https://doi.org/10.1038/s41592-025-02865-2

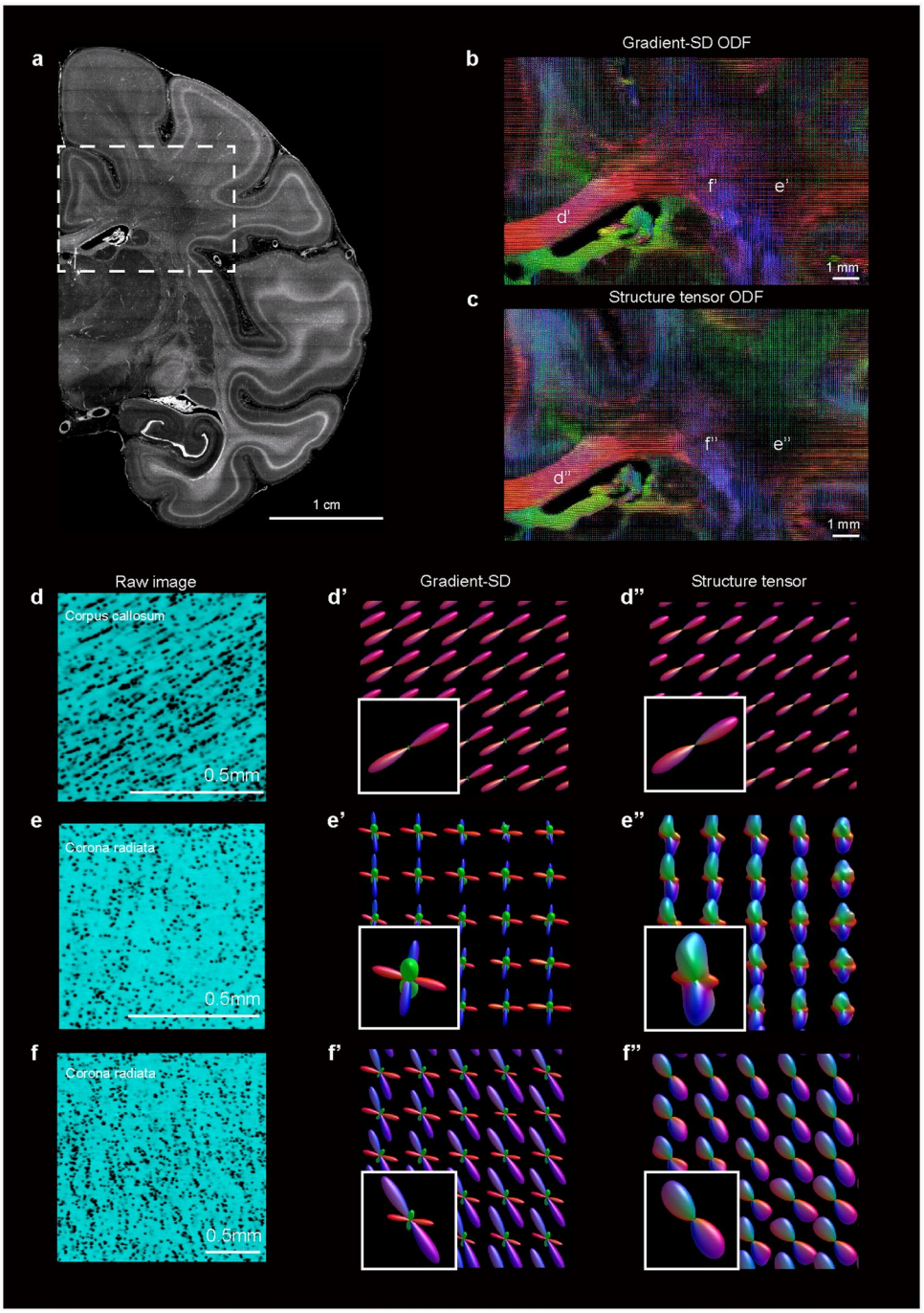

Extended Data Fig. 2 | Comparison of orientation detection methods based on image gradient or structure tensor in the fiber-crossing regions. (**a**) A raw Nissl-stained section of a macaque hemibrain. (**b**-**c**) Visualization of cODFs in the area within the white rectangle in (**a**) by our gradient-based method (**b**) and the structure tensor (ST)-based method (**c**), showing similar results at the macroscopic scale. (**d**-**f**) Magnified views of the regions indicated in (**b**-**c**) and their corresponding raw images. The left column presents raw image within corpus callosum (**d**) and corona radiata (**e**-**f**). The middle and right columns show the gradient-ODFs (**d'**-**f'**) and ST-ODFs (**d''**-**f''**). Each ST-ODF gathered ST orientations in a region of 80×80×80 μm^3, where each ST was calculated from a nonoverlapping 16×16×16 μm^3 window.

https://doi.org/10.1038/s41592-025-02865-2

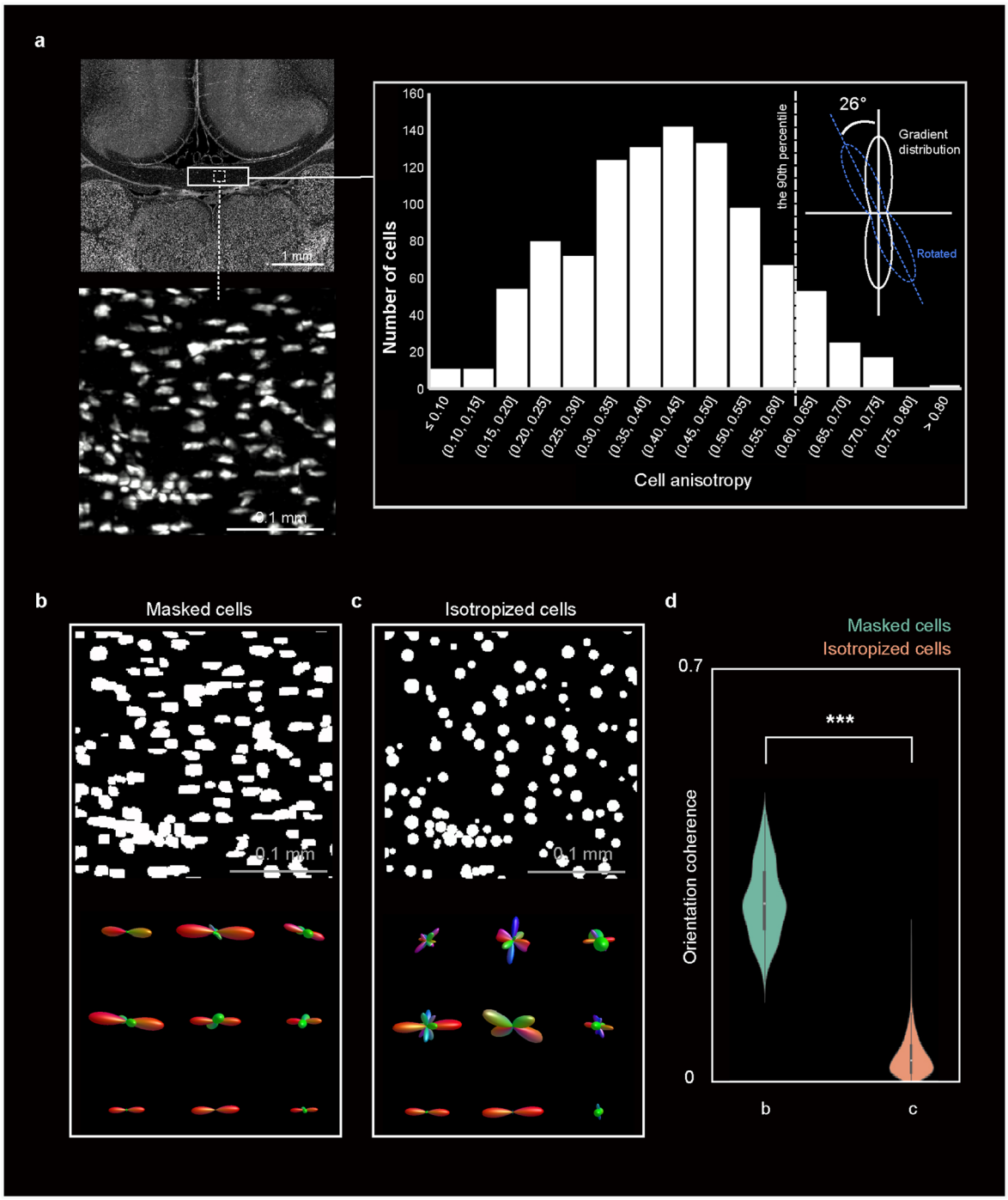

Extended Data Fig. 3 | Anisotropic cellular shape substantially contributes to cytoarchitectonic orientation estimation. (**a**) An image of the marmoset corpus callosum, with a bar plot showing the distribution of cellular anisotropy within a representative local region. Fractional anisotropy was computed from ellipsoid-fitted cell masks. The inset illustrates the gradient distribution for a cell with FA = 0.6 (90th percentile), and that after rotated by the half-maximum width (~ 26°, in blue). (**b**) Binary mask of segmented cells in the original image. (**c**) Simulated data in which each segmented cell is replaced by a sphere of equal volume, keeping their spatial positions unchanged. (**d**) Comparison of orientation coherence between (**b**) and (**c**), assessed via structure tensor analysis. ***, $P < 0.001$, $n = 98{,}587$ sliding analysis windows, two-sided Mann-Whitney U test, $p <$ 1e-300.

https://doi.org/10.1038/s41592-025-02865-2

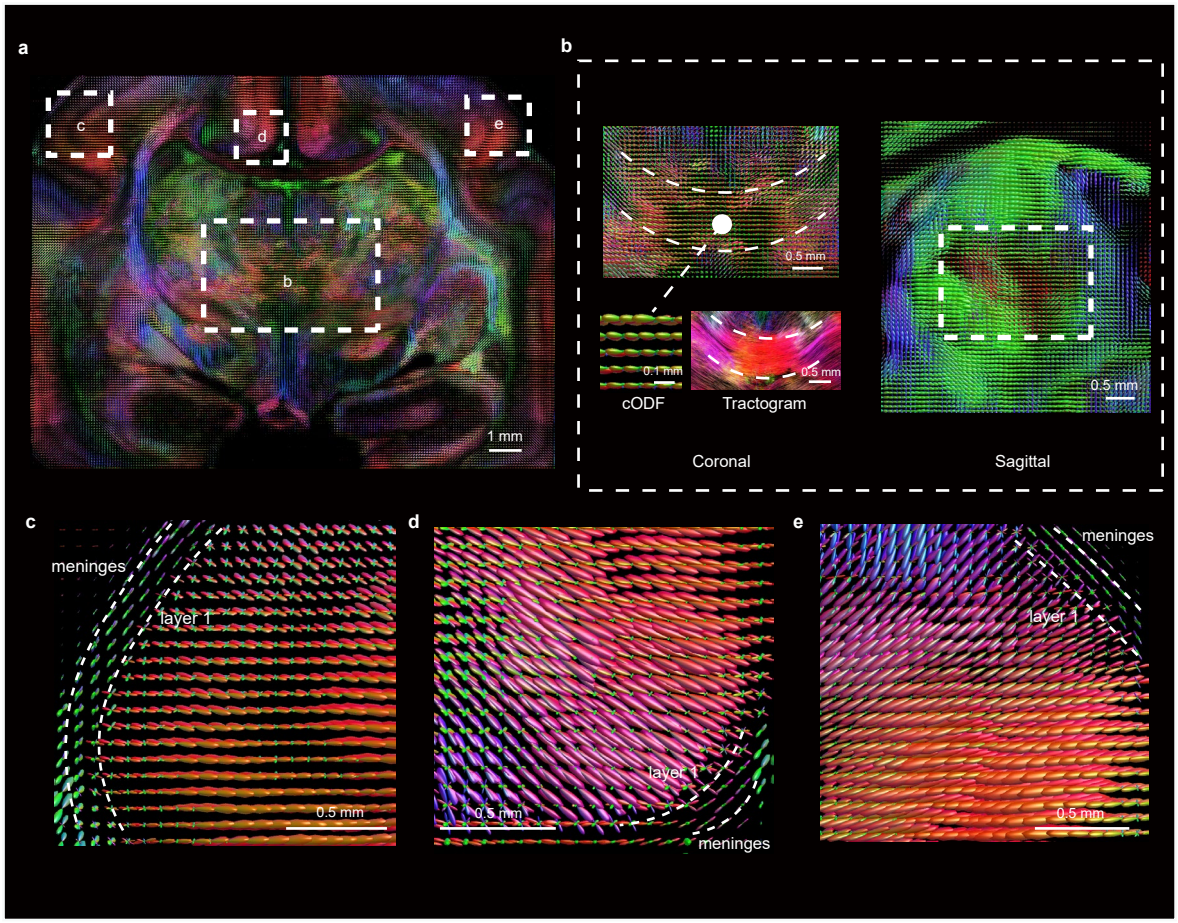

Extended Data Fig. 4 | CABLE analysis of the thalamus and cortex of a newborn marmoset. (**a**) A coronal-section view of cODFs derived from a newborn marmoset. (**b**) Enlarged coronal view of the thalami (upper left) with CABLE tractography (lower left) and the corresponding sagittal view (right). The dashed lines indicate the direction of the left-right fibers of the thalamus. (**c-e**) Enlarged views of several cortical areas. Dashed lines indicate the border of the meninges and cortical layer I.

https://doi.org/10.1038/s41592-025-02865-2

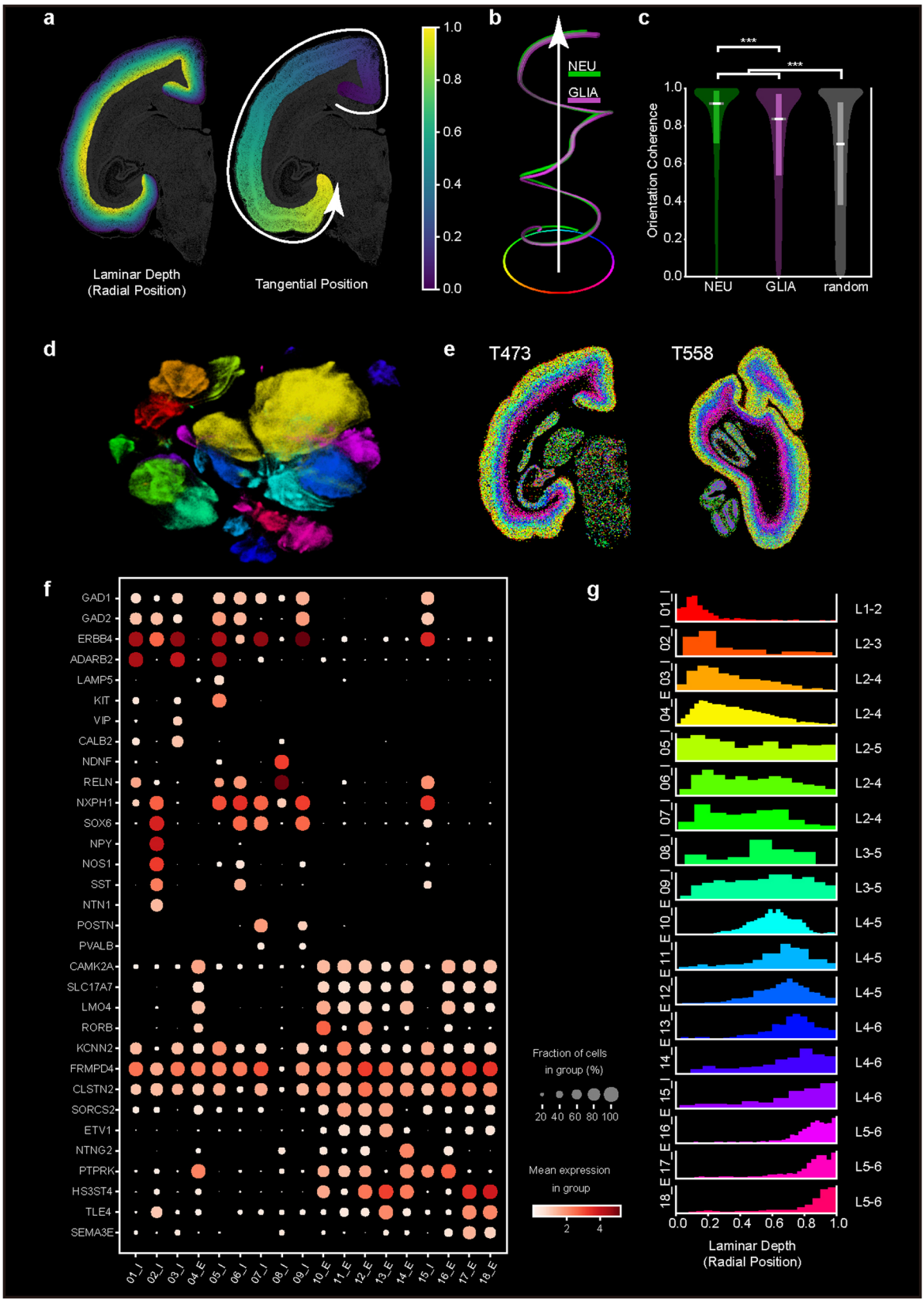

Extended Data Fig. 5 | See next page for caption.

https://doi.org/10.1038/s41592-025-02865-2

Extended Data Fig. 5 | Orientation coherence analysis and neuron subtype classification on the cortical area. (**a**) Illustration showing the color mapping of relative radial position (laminar depth) and tangential position in the cortex region of T472 marmoset brain section. (**b**) 3D lines depicting the median orientations of neurons and glial cells changing similarly along the tangential axis. Each position on the 3D line represents a tangential position along the ascending tangential axis and the cellular orientation at that position, which is indicated by its projection to the bottom circle. (**c**) Violin plot showing significant high orientation coherence in both cortical neurons (NEU) and glial cells (GLIA), while the cortical neurons have a higher orientation coherence. n = 31,980 (NEU), n = 13,503 (GLIA). *** indicates $P < 0.001$ with two-sided Mann–Whitney U-test between NEU and GLIA, and between NEU/GLIA groups and the simulation group (random), n = 31,980 [NEU], 13,503 [GLIA], 254,530 [random]; P = 6.16e-178 [NEU-GLIA], less than 1.00e-300 [NEU-random], 2.22e-263 [GLIA-random]. The embedded box plots in violin plots indicate the median (central white horizontal line) and the interquartile range (25th and 75th percentiles, box edges). Whiskers, minima and maxima outside this range are not shown. (**d**) UMAP scatter plot of cortical neuron subtypes. The single-nucleus RNA sequencing dataset was used for the annotation of subtypes on spatial transcriptome sections. Each neuron subtype is colored according to its preferred laminar depth distribution as indicated in (**g**). (**e**) Mapping of neuron subtypes (01_I to 18_E) on spatial transcriptome slices T473 and T558. (**f**) Dot plot showing marker gene expression profiles of each neuron subtype (numbered from 01 to 18, and E for excitatory neurons and I for inhibitory neurons). (**g**) Relative radial position distribution (layer 1 to layer 6, L1-L6) of all neuron subtypes.

https://doi.org/10.1038/s41592-025-02865-2

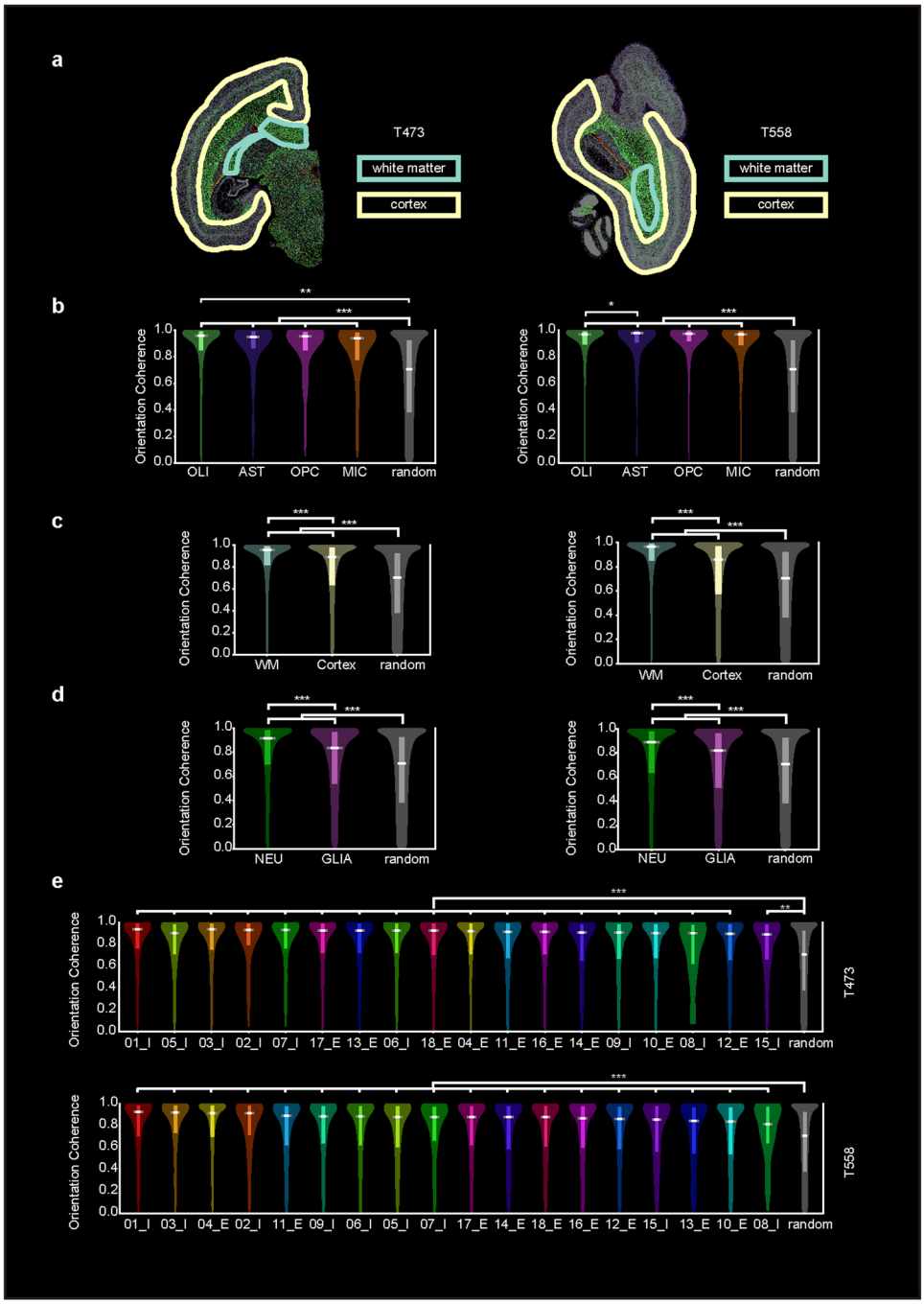

Extended Data Fig. 6 | See next page for caption.

https://doi.org/10.1038/s41592-025-02865-2

Extended Data Fig. 6 | Orientation coherence analysis in sections T473 and T558. (**a**) Contours of manually segmented cortex and white matter. (**b**) Violin plots showing high orientation coherence of all four glial cell types in segmented white matter regions. (**c**) Violin plots showing high orientation coherence of both white matter cells and cortical cells, while the cortical cytoarchitectonic orientation coherence is lower than the white matter (WM). (**d**) Violin plots showing high orientation coherence in both cortical neurons (NEU) and glial cells (GLIA), while the cortical neurons have a higher orientation coherence than glial cells. (**e**) Distribution of orientation coherence for neuron subtypes with null model comparisons, calculated from section T473 and T558. In (**b**-**e**), * $P < 0.05$, ** $P < 0.01$ and *** $P < 0.001$ (two-sided Mann–Whitney U-test). For the section T473, n = 4,966 [OLI], 134 [AST], 142 [OPC], 173 [MIC], 10,472 [WM], 103,070 [Cortex], 32,747 [NEU], 13,286 [GLIA], 684 [01_I], 766 [05_I], 870 [03_I], 137 [02_I], 412 [07_I], 1,751 [17_E], 704 [13_E], 1,723 [06_I], 875 [18_E], 12,499 [04_E], 587 [11_E], 2,011 [16_E], 561 [14_E], 1,745 [09_I], 4,995 [10_E], 57 [08_I], 2,035 [12_E], 321 [15_I], 238,500 [random]; P values (vs. random unless noted): <1.0e-300 [OLI], 2.6e-23 [AST], 2.9e-22 [OPC], 2.6e-21 [MIC], 5.8e-01 [OLI-AST], 3.0e-01 [OLI-OPC], 8.3e-03 [OLI-MIC], 6.6e-01 [AST-OPC], 1.5e-01 [AST-MIC], 3.3e-01 [OPC-MIC], 3.2e-242 [WM-Cortex], less than 1.0e-300 [WM], less than 1.0e-300 [Cortex], 2.9e-167 [NEU-GLIA], <1.0e-300 [NEU], 1.8e-250 [GLIA], 3.3e-69 [01_I], 2.6e-54 [05_I], 4.4e-84 [03_I], 4.8e-15 [02_I], 3.4e-40 [07_I], 1.0e-138 [17_E], 7.5e-60 [13_E], 4.3e-133 [06_I], 8.1e-67 [18_E], <1.0e-300 [04_E], 3.0e-41 [11_E], 1.6e-144 [16_E], 6.7e-36 [14_E], 7.4e-105 [09_I], 5.4e-282 [10_E], 1.5e-03 [08_I], 4.9e-110 [12_E], 5.4e-19 [15_I]. For the section T558, n = 5,490 [OLI], 224 [AST], 265 [OPC], 208 [MIC], 13,120 [WM], 182,721 [Cortex], 61,452 [NEU], 19,011 [GLIA], 955 [01_I], 1,299 [03_I], 23,175 [04_E], 224 [02_I], 1,262 [11_E], 3,276 [09_I], 3,036 [06_I], 1,249 [05_I], 724 [07_I], 3,596 [17_E], 1,652 [14_E], 2,195 [18_E], 3,512 [16_E], 3,986 [12_E], 592 [15_I], 1,351 [13_E], 9,048 [10_E], 265 [08_I], 480,791 [random]; p values (vs. random unless noted): <1.0e-300 [OLI], 8.3e-54 [AST], 1.4e-66 [OPC], 1.0e-44 [MIC], 4.1e-02 [OLI-AST], 9.3e-02 [OLI-OPC], 5.2e-01 [OLI-MIC], 7.3e-01 [AST-OPC], 5.0e-02 [AST-MIC], 9.0e-02 [OPC-MIC], <1.0e-300 [WM-Cortex], less than 1.0e-300 [WM], less than 1.0e-300 [Cortex], 7.4e-145 [NEU-GLIA], <1.0e-300 [NEU], 1.2e-257 [GLIA], 3.5e-72 [01_I], 4.5e-106 [03_I], <1.0e-300 [04_E], 1.3e-16 [02_I], 8.6e-57 [11_E], 1.5e-140 [09_I], 5.2e-127 [06_I], 3.2e-48 [05_I], 5.2e-36 [07_I], 1.9e-143 [17_E], 2.5e-58 [14_E], 7.0e-85 [18_E], 4.5e-121 [16_E], 1.9e-124 [12_E], 3.6e-19 [15_I], 4.5e-31 [13_E], 4.9e-178 [10_E], 5.2e-09 [08_I]. The embedded box plots in violin plots indicate the median (central white horizontal line) and the interquartile range (25th and 75th percentiles, box edges). Whiskers, minima and maxima outside this range are not shown.

https://doi.org/10.1038/s41592-025-02865-2

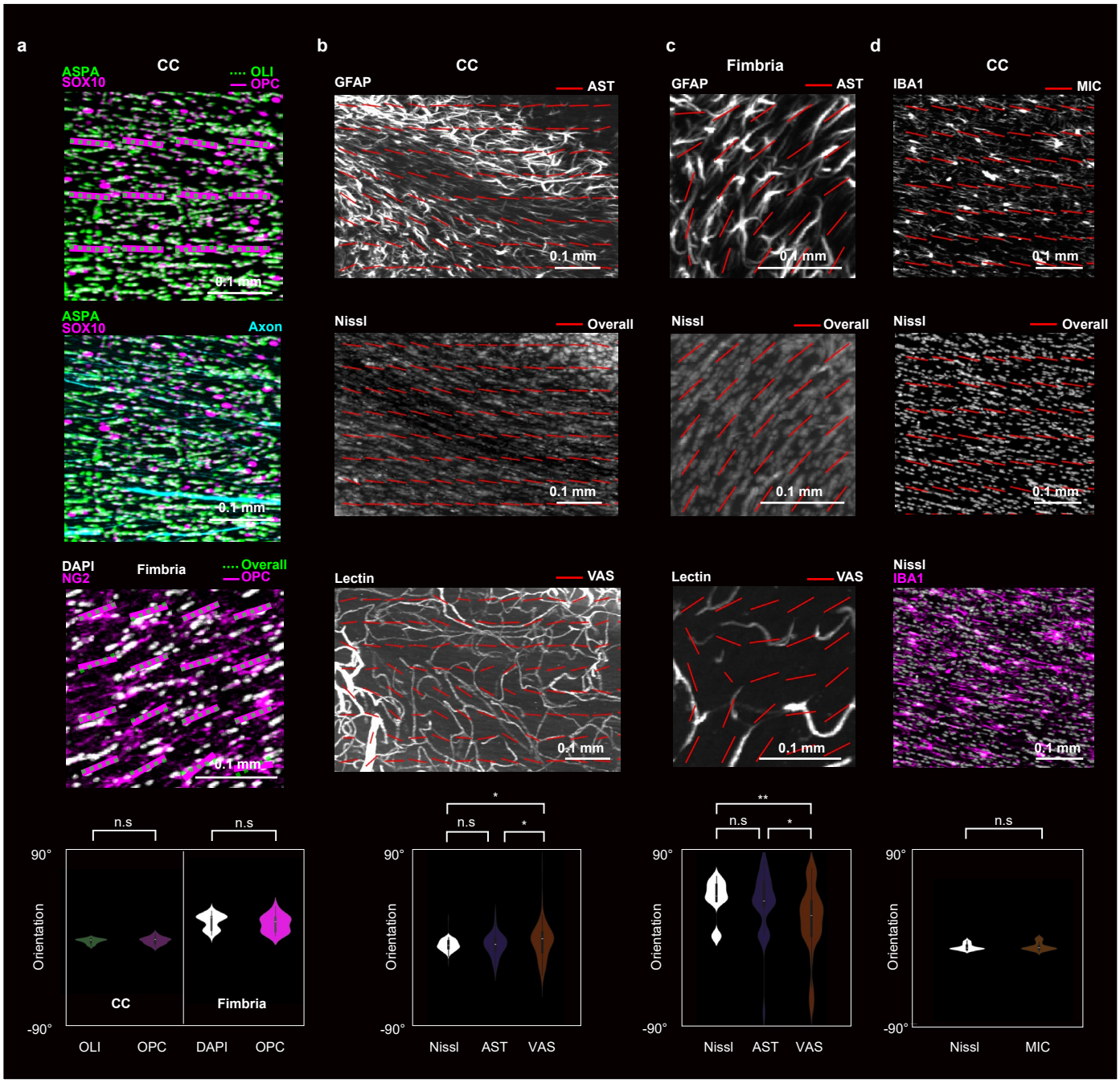

Extended Data Fig. 7 | Various types of glial cells exhibit coherent alignment with cytoarchitectonic orientation. (**a**) First row: Co-staining of ASPA (green; mature oligodendrocyte marker) and SOX10 (magenta; marker of all oligodendrocyte lineage cells) in the mouse corpus callosum (CC); Second row: ASPA/SOX10 images merged with virus-labeled axons in cyan. Cells positive for SOX10 but negative for ASPA (magenta only) are presumptive OPCs. Third row: Co-staining of NG2 (magenta; direct OPC marker) and DAPI (white) in the mouse fimbria. Magenta and green dotted lines indicate the local orientations of OPCs ($SOX10^+/ASPA^-$ or $NG2^+$) and overall cell populations ($SOX10^+$ or $DAPI^+$), respectively. Fourth row: Quantification of orientation coherence in the CC and fimbria shows no significant difference between OPCs and mature oligodendrocytes in the CC ($P = 0.54$, $n = 20$), or between OPCs and DAPI-labeled nuclei in the fimbria ($P = 0.66$, $n = 25$). (**b**–**c**) Co-staining of GFAP (astrocytes), Nissl, and Lectin (vasculature) in the mouse CC (**b**) and fimbria (**c**). Red line segments indicate local orientations derived from astrocytes (AST), Nissl (Overall), and vasculature (VAS). No significant difference was observed between AST and Nissl in either region ($P = 0.43$, $n = 117$ for CC; $P = 0.38$, $n = 30$ for fimbria). AST and VAS orientations differed slightly in the CC ($P = 0.04$, $n = 117$) and fimbria ($P = 0.03$, $n = 30$). VAS and Nissl orientations were significantly different in both CC ($P = 0.002$, $n = 117$) and fimbria ($P = 0.003$, $n = 30$). (**d**) Co-staining of IBA1 (microglia) and Nissl in the mouse CC. Red line segments indicate local orientations of microglia (MIC) and Nissl-inferred overall orientation. No significant difference was found between MIC and Nissl orientations ($P = 0.55$, $n = 64$). Two-sided Mann–Whitney U tests were used for all statistical comparisons. Violin plots show the distribution of orientation values using kernel density estimation. The embedded box plots indicate the median (central line), the interquartile range (25th and 75th percentiles; box edges), and the whiskers represent data within 1.5×IQR from the quartiles. Minima and maxima outside this range are not shown.

https://doi.org/10.1038/s41592-025-02865-2

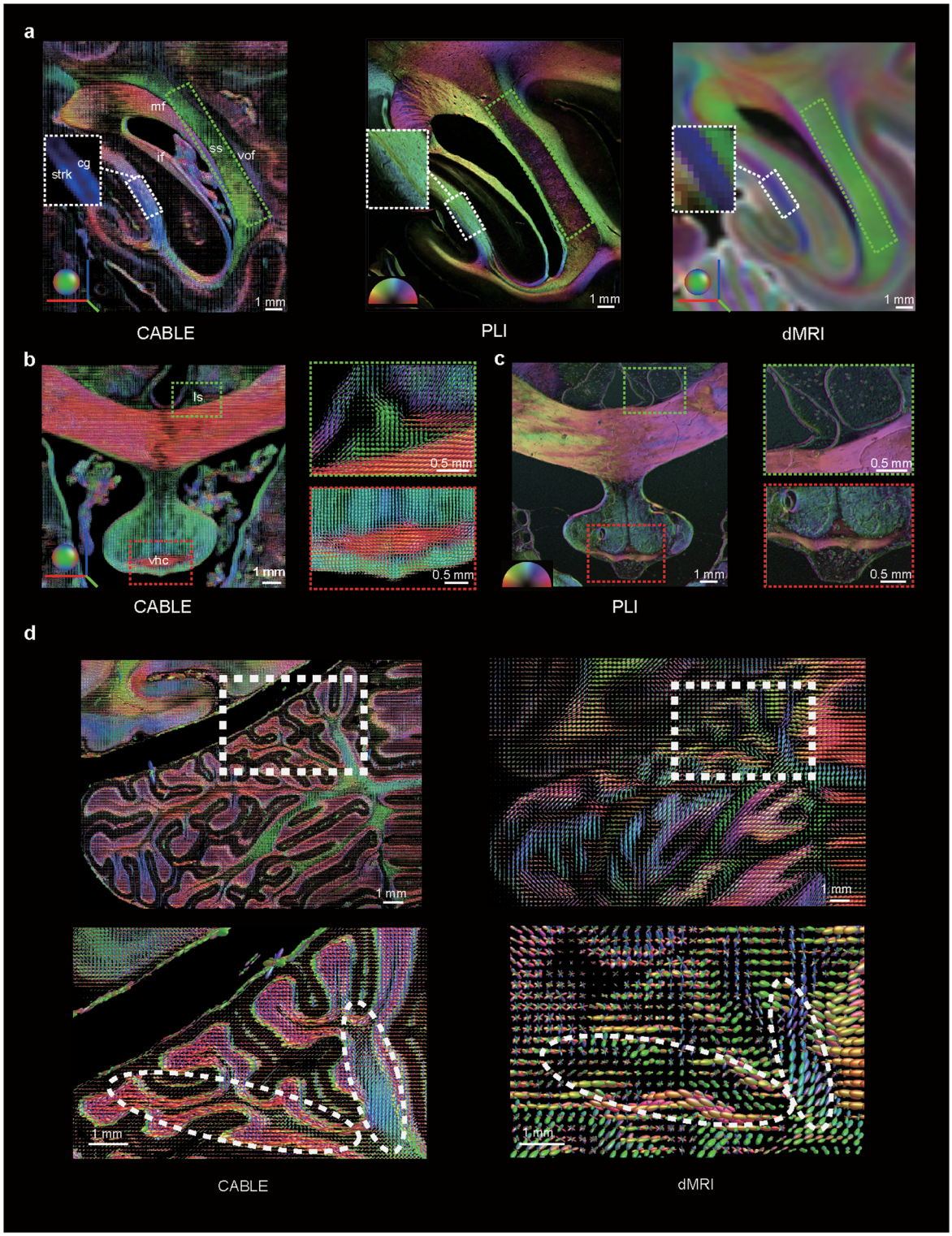

Extended Data Fig. 8 | Comparison of CABLE with other methods for macaque brain mapping. (**a**) Comparative visualization of occipital white matter fiber architecture using CABLE, PLI, and dMRI techniques. CABLE (left) delineates distinct white matter structures (medial to lateral): stratum calcarinum (strk), cingulum (cg), inferior forceps (if), forceps major (mf), sagittal stratum (ss), and vertical occipital fasciculus (vof). In dMRI images, the gap between strk and cg is hardly discernible. (**b-c**) Depiction of the ventral hippocampal commissure (vhc; red box) and medial longitudinal striae (ls; green box) by CABLE (b) and PLI (c). (**d**) Representative images of CABLE and dMRI ODFs in the macaque cerebellum. The lower row presents magnified views of the areas outlined in the upper row.

https://doi.org/10.1038/s41592-025-02865-2

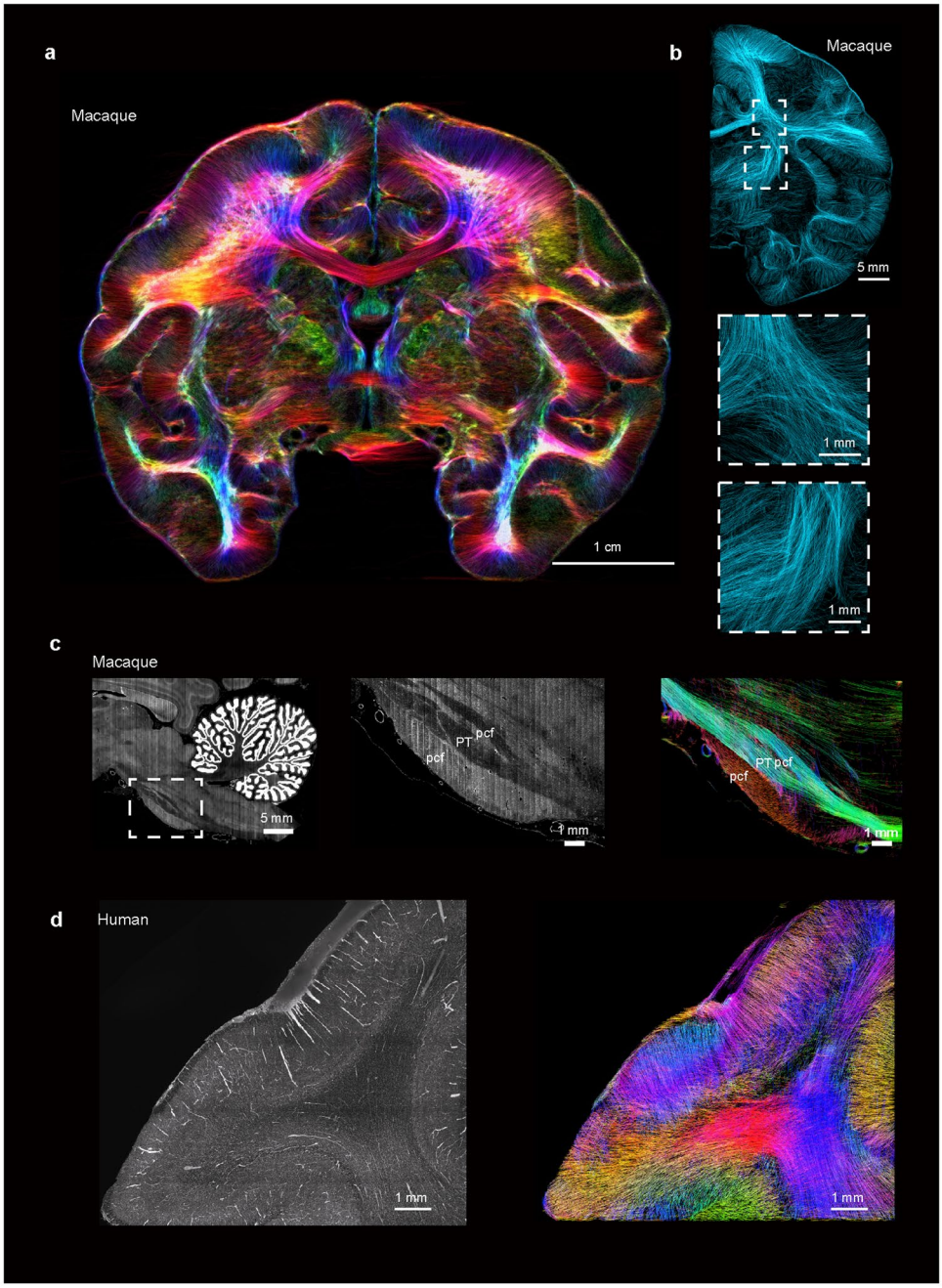

Extended Data Fig. 9 | CABLE-derived tractograms in the rhesus monkey and human brains. (**a**) Coronal view of a CABLE-derived tractogram in the macaque brain. (**b**) Tractogram of another coronal section of macaque brain, highlighting the corona radiata (middle) and internal capsule (lower). (**c**) Sagittal view of DAPI-stained macaque brainstem (left) with the box region enlarged (middle). Corresponding CABLE-derived tractogram (right) illustrates the interweaving between the pyramidal tract (PT) and the preculminate fissure (pcf). (**d**) Coronal view of an adult human brain tissue block from epilepsy surgery (left) and its corresponding CABLE-derived tractogram (right).

nature portfolio

Corresponding author(s): Fang Xu, Cirong Liu, Yanyang Xiao, Guo-Qiang Bi

Last updated by author(s): Jul 8, 2025

Reporting Summary

Nature Portfolio wishes to improve the reproducibility of the work that we publish. This form provides structure for consistency and transparency in reporting. For further information on Nature Portfolio policies, see our Editorial Policies and the Editorial Policy Checklist.

Statistics

For all statistical analyses, confirm that the following items are present in the figure legend, table legend, main text, or Methods section.

n/a	Confirmed	
☐	☒	The exact sample size (*n*) for each experimental group/condition, given as a discrete number and unit of measurement
☐	☒	A statement on whether measurements were taken from distinct samples or whether the same sample was measured repeatedly
☐	☒	The statistical test(s) used AND whether they are one- or two-sided *Only common tests should be described solely by name; describe more complex techniques in the Methods section.*
☒	☐	A description of all covariates tested
☒	☐	A description of any assumptions or corrections, such as tests of normality and adjustment for multiple comparisons
☐	☒	A full description of the statistical parameters including central tendency (e.g. means) or other basic estimates (e.g. regression coefficient) AND variation (e.g. standard deviation) or associated estimates of uncertainty (e.g. confidence intervals)
☐	☒	For null hypothesis testing, the test statistic (e.g. *F*, *t*, *r*) with confidence intervals, effect sizes, degrees of freedom and *P* value noted *Give P values as exact values whenever suitable.*
☒	☐	For Bayesian analysis, information on the choice of priors and Markov chain Monte Carlo settings
☒	☐	For hierarchical and complex designs, identification of the appropriate level for tests and full reporting of outcomes
☒	☐	Estimates of effect sizes (e.g. Cohen's *d*, Pearson's *r*), indicating how they were calculated

Our web collection on statistics for biologists contains articles on many of the points above.

Software and code

Policy information about availability of computer code

Data collection	The data acquisition software in companion with the commercial VISoR2 imaging system were used to collect whole-brain images used in this study.
Data analysis	The code and installation guide for CABLE analysis can be found at the Github repository (https://github.com/BrainCABLE). As described in the installation guide, we use MRtrix3 (v3.0.4) for constrained spherical deconvolution(CSD) and visualization of fiber tracks, which can be accessed via https://www.mrtrix.org/download/.

For manuscripts utilizing custom algorithms or software that are central to the research but not yet described in published literature, software must be made available to editors and reviewers. We strongly encourage code deposition in a community repository (e.g. GitHub). See the Nature Portfolio guidelines for submitting code & software for further information.

Data

Policy information about availability of data

All manuscripts must include a data availability statement. This statement should provide the following information, where applicable:

- Accession codes, unique identifiers, or web links for publicly available datasets
- A description of any restrictions on data availability
- For clinical datasets or third party data, please ensure that the statement adheres to our policy

The complete image datasets for macaque, marmoset, human, and mouse brains exceed 300 terabytes in total size and are therefore impractical to upload in full to

a public data repository. A subset of the data is available at https://cable.bigconnectome.org, including: demo datasets for testing the CABLE analysis code; a representative slice image of the macaque brain (RM009) used in Fig. 1c; the Stereo-seq dataset analyzed in Fig. 2, Extended Data Figs. 5 and 6, and Supplementary Figs. 9–11; and a multimodal marmoset brain dataset (CJ004) used in Figs. 3 and 4. Additional datasets related to any figure or video in this work are available from the corresponding author upon reasonable request, using feasible data transfer methods such as physical hard drives, cloud storage, or on-site access.

Research involving human participants, their data, or biological material

Policy information about studies with human participants or human data. See also policy information about sex, gender (identity/presentation), and sexual orientation and race, ethnicity and racism.

Reporting on sex and gender	This study included a 19-day-old male newborn brain and a male brain tissue block obtained from epilepsy surgery.
Reporting on race, ethnicity, or other socially relevant groupings	Not applicable.
Population characteristics	Not applicable.
Recruitment	Brain tissue of the newborn and the epilepsy surgery were obtained from the National Health and Disease Human Brain Tissue Resource Center, Anhui Medical University (NBC-AMU). Informed consent for autopsy and the use of body material was approved by the parents.
Ethics oversight	The experimental procedures were approved by the Anhui Provincial Children's Hospital Medical Research Ethics Committee (No. EYLL-2024-048).

Note that full information on the approval of the study protocol must also be provided in the manuscript.

Field-specific reporting

Please select the one below that is the best fit for your research. If you are not sure, read the appropriate sections before making your selection.

☒ Life sciences ☐ Behavioural & social sciences ☐ Ecological, evolutionary & environmental sciences

For a reference copy of the document with all sections, see nature.com/documents/nr-reporting-summary-flat.pdf

Life sciences study design

All studies must disclose on these points even when the disclosure is negative.

Sample size	Three macaque brains and six marmoset brains for whole-brain multi-channel imaging, reconstruction and tracing. A human brain and a mouse brain were used for study of HIE. More than 5 mice brain were used for immunostaining.
Data exclusions	No data was excluded from the analyses.
Replication	We performed replicate experiments in normal brains of the mouses, macaques and marmosets, for whole-brain image acquisition based on the validation experiment. The replicates were consistent in data quality and cytoarchitectonic organization.
Randomization	Monkeys and mice were randomly selected for injection and imaging purposes.
Blinding	The investigators were blinded to group allocation during data collection and analysis where grouping is required.

Reporting for specific materials, systems and methods

We require information from authors about some types of materials, experimental systems and methods used in many studies. Here, indicate whether each material, system or method listed is relevant to your study. If you are not sure if a list item applies to your research, read the appropriate section before selecting a response.

Materials & experimental systems

n/a	Involved in the study
☐	☒ Antibodies
☒	☐ Eukaryotic cell lines
☒	☐ Palaeontology and archaeology
☐	☒ Animals and other organisms
☒	☐ Clinical data
☒	☐ Dual use research of concern
☒	☐ Plants

Methods

n/a	Involved in the study
☒	☐ ChIP-seq
☒	☐ Flow cytometry
☐	☒ MRI-based neuroimaging

Antibodies

Antibodies used: Detailed information on all primary and secondary antibodies used in this study, including species, supplier, catalog number, and working dilutions, is provided in Supplementary Tables 2 and 3.

Validation: All primary and secondary antibodies were validated by the manufacturers for use in immunofluorescence staining in mouse or marmoset tissues. Validation was confirmed via manufacturer datasheets and supported by staining specificity consistent with known expression profiles. Full antibody details are listed in Supplementary Tables 2 and 3.

Animals and other research organisms

Policy information about studies involving animals; ARRIVE guidelines recommended for reporting animal research, and Sex and Gender in Research

Laboratory animals: Six common marmosets (Callithrix jacchus) were used in this study. CJ001, a 3-year-old male marmoset, was used to obtain coronal sections for Stereo-seq. CJ003, a 3-year-old male marmoset, was used to obtain sagittal sections for Stereo-seq as biological replication. CJ002, a 5-year-old female marmoset, was used for hippocampus interhemispheric projection labeling. CJ004, a 7.5-year-old male marmoset, was used for crossing-BBB viral labeling. CJ005 was a newborn marmoset, used for white matter development analysis. Three adult, 10-year-old, male rhesus macaques (Macaca mulatta) were used in this study. More than 5 male C57BL/6J mice were used in this study for immunostaining experiments, housing under a 12-hour light/dark cycle and with free access to food and water. Neonatal hypoxia-ischemia models were used to mimic the neonatal human HIE.

Wild animals: This study did not involve wild animals.

Reporting on sex: This study was not limited to a single gender and gender was not considered in the experimental design.

Field-collected samples: This study did not involve samples collected from the field.

Ethics oversight: Center for Excellence in Brain Science & Intelligence Technology (CEBSIT); Chinese Academy of Sciences; Kunming Institute of Zoology (KIZ), Chinese Academy of Sciences; Shenzhen Institutes of Advanced Technology (SIAT), Chinese Academy of Sciences.

Note that full information on the approval of the study protocol must also be provided in the manuscript.

Plants

Seed stocks: Not applicable.

Novel plant genotypes: Not applicable.

Authentication: Not applicable.

Magnetic resonance imaging

Experimental design

Design type: Structural imaging

Design specifications: Not relevant as this study did not use functional MRI methods.

Behavioral performance measures: This study only involved ex vivo scanning.

Acquisition

Imaging type(s): Diffusion MRI

Field strength: 9.4T

Sequence & imaging parameters: The brain sample of marmoset CJ004 was scanned using 3-D diffusion-weighted multi-shot spin-echo echo planar imaging (EPI) sequence on a 9.4T/12-cm MRI (Bruker Biospin), equipped with a 35-mm birdcage volume coil. The acquisition parameters were set as follows: repetition time (TR) = 165 ms, echo time (TE) = 23.4428, number of segments = 24, field of view (FOV) = 26.4 × 34.2 × 19.2, and matrix size = 176 × 168 × 128, resulting in a spatial resolution of 150 µm isotropic.

Area of acquisition: Whole brian

Diffusion MRI ☒ Used ☐ Not used

Parameters: In total, 96 diffusion-weighted images (DWI) were collected, comprising 6 b = 0 s/mm2, 60 b = 1500 s/mm2, and 30 b = 3000 s/mm2.

Preprocessing

Preprocessing software: MRtrix3(v3.04) and FSL(v6.0) were used in this study.

Normalization: The dMRI data was not registered to a group template.

Normalization template: Not applicable.

Noise and artifact removal: The dMRI data was denoised using Marchenko-Pastur PCA, implemented by the dwidenoise function of MRtrix3.

Volume censoring: Not applicable.

Statistical modeling & inference

Model type and settings: Not applicable.

Effect(s) tested: Not applicable.

Specify type of analysis: ☒ Whole brain ☐ ROI-based ☐ Both

Statistic type for inference (See Eklund et al. 2016): Not applicable. This study did not require inferences.

Correction: The data were eddy-corrected using the eddy_correct function in FSL.

Models & analysis

n/a	Involved in the study
☒	☐ Functional and/or effective connectivity
☒	☐ Graph analysis
☒	☐ Multivariate modeling or predictive analysis